#### T CELLS

## Single-cell topographical profiling of the immune synapse reveals a biomechanical signature of cytotoxicity

Miguel de Jesus<sup>1</sup>†, Alexander H. Settle<sup>1</sup>†, Daan Vorselen<sup>2,3</sup>, Thomas K. Gaetjens<sup>4</sup>, Michael Galiano<sup>5</sup>, Yevgeniy Romin<sup>5</sup>, Esther Lee<sup>6</sup>, Yung Yu Wong<sup>1</sup>, Tian-Ming Fu<sup>7</sup>, Endi Santosa<sup>6</sup>, Benjamin Y. Winer<sup>8</sup>, Fella Tamzalit<sup>8</sup>, Mitchell S. Wang<sup>9</sup>, Anthony Santella<sup>5</sup>, Zhirong Bao<sup>10</sup>, Joseph C. Sun<sup>8</sup>, Pavak Shah<sup>11</sup>, Julie A. Theriot<sup>3</sup>, Steven M. Abel<sup>4</sup>, Morgan Huse<sup>8</sup>\*

Immune cells have intensely physical lifestyles characterized by structural plasticity and force exertion. To investigate whether specific immune functions require stereotyped mechanical outputs, we used super-resolution traction force microscopy to compare the immune synapses formed by cytotoxic T cells with contacts formed by other T cell subsets and by macrophages. T cell synapses were globally compressive, which was fundamentally different from the pulling and pinching associated with macrophage phagocytosis. Spectral decomposition of force exertion patterns from each cell type linked cytotoxicity to compressive strength, local protrusiveness, and the induction of complex, asymmetric topography. These features were validated as cytotoxic drivers by genetic disruption of cytoskeletal regulators, live imaging of synaptic secretion, and in silico analysis of interfacial distortion. Synapse architecture and force exertion were sensitive to target stiffness and size, suggesting that the mechanical potentiation of killing is biophysically adaptive. We conclude that cellular cytotoxicity and, by implication, other effector responses are supported by specialized patterns of efferent force.



Copyright © 2024 Authors, some rights reserved; exclusive licensee American Association for the Advancement of Science. No claim to original U.S. Government Works

#### **INTRODUCTION**

Life on all scales is rooted as deeply in mechanics as it is in chemistry (1-3). This is particularly true of the immune system, which carries out its functions in diverse mechanochemical environments ranging from fluids (e.g., blood and lymph) and soft tissues like the lung and liver to stiffer tissues like muscle and bone (4, 5). Within each of these environments, individual immune cells interact with a variety of other cells, the extracellular matrix, and occasionally foreign pathogens (6, 7). To interpret and respond to this complexity, immune cells have evolved to be structurally plastic, dynamically changing shape to transit between different tissues, and to be physically active, imparting force against their surroundings. Force exertion enables immune cells to sense physical parameters like rigidity and pressure, which influences their activation state (8-11), gene expression (12), metabolism (13, 14), and mesoscale cell behaviors (15-17).

Immune cells also use force exertion to manipulate cells and other objects in their environment, typically through dynamic, structurally stereotyped interactions (6). During macrophage phagocytosis, for example, interfacial force powers the adhesion of integrins and

<sup>1</sup>Louis V. Gerstner, Jr., Graduate School of Biomedical Sciences, Memorial Sloan Kettering Cancer Center, New York, NY, USA. <sup>2</sup>Cell Biology and Immunology Group, Wageningen University & Research, Wageningen, Netherlands. <sup>3</sup>Department of Biology, University of Washington, Seattle, WA, USA. <sup>4</sup>Department of Chemical and Biomolecular Engineering, University of Tennessee, Knoxville, TN, USA. Molecular Cytology Core Facility, Memorial Sloan Kettering Cancer Center, New York, NY, USA. <sup>6</sup>Immunology & Molecular Pathogenesis Program, Weill Cornell Medicine Graduate School of Medical Sciences, New York, NY, USA. <sup>7</sup>Department of Electrical and Computer Engineering, Princeton University, Princeton, NJ, USA. 8Immunology Program, Memorial Sloan Kettering Cancer Center, New York, NY, USA. 9Pharmacology Program, Weill Cornell Medicine Graduate School of Medical Sciences, New York, NY, USA.  $^{10}$ Developmental Biology Program, Memorial Sloan Kettering Cancer Central Control of the Control ter, New York, NY, USA. 11 Department of Molecular, Cell, and Developmental Biology, University of California Los Angeles, Los Angeles, CA, USA.

\*Corresponding author. Email: husem@mskcc.org †These authors contributed equally to this work.

other uptake receptors, the detachment and/or fragmentation of cargo, and phagocytic cup closure (18-21). Recent mechanical profiling studies have revealed elaborate patterns of protrusive and tangential force exertion within the phagocytic cup, including the formation of peripheral structures that appear to facilitate gripping by "biting" the cargo (22). Force plays distinct but no less important roles in lymphocyte contacts, where it modulates antigen acquisition by B cells and killing of infected or transformed target cells by CD8+ cytotoxic T lymphocytes (CTLs) (23–26). In the case of CTLs, force potentiates the efficacy of a targeted secretory response, namely, the release of perforin and granzymes through the cytolytic immune synapse. Once secreted, perforin oligomerizes to form pores in the target membrane that enable granzymes to access the cytoplasm, where they proteolytically induce apoptosis (27, 28). Prior studies suggest that CTL-derived forces not only dictate where within the synapse perforin and granzyme are released (29) but also facilitate perforin pore formation by straining the target cell surface (26). The basis for this physicochemical synergy remains poorly understood but has been linked to the formation of filamentous (F)-actin-based protrusions within the synapse (30).

Together, this prior research suggests both that immune cells use interfacial force to potentiate their effector responses and that force exertion is tailored to the specific purpose of each interface. As such, it is tempting to speculate that different immune lineages and even functionally distinct subsets within the same lineage might generate distinguishable patterns of force exertion. To explore this hypothesis, we applied a super-resolution traction force microscopy (TFM) approach that uses deformable polyacrylamide microparticles to visualize synaptic forces in three dimensions (20). By comparing the mechanical outputs of CTLs with functionally distinct T cell subsets as well as macrophages, we were able to identify a specialized pattern of interfacial force, or mechanotype, distinguishing cytolytic synapses from other types of interactions.

#### **RESULTS**

#### CTLs actively compress and micropattern their targets

To profile synapse mechanics, we used a three-dimensional (3D) TFM system in which T cells were induced to form synapses with deformable polyacrylamide-acrylic acid microparticles (DAAM particles) (20). DAAM particles (13  $\mu$ m in diameter) with a stiffness (Young's modulus) of 300 Pa were functionalized with intercellular adhesion molecule–1 (ICAM-1), a ligand for the  $\alpha_L\beta_2$  integrin LFA-1, and either anti-CD3 $\epsilon$  antibody or a class I peptide-major histocompatibility complex (pMHC) specific for the OT-1 or P14 T cell receptor (TCR) (Fig. 1A). OT-1 and P14 CTLs both formed physically active synapses with these stimulatory DAAM particles, which we imaged using high-speed structured illumination microscopy (31). 3D triangulation of each particle surface enabled us to visualize the physical deformations induced by the CTL synapse at sub-micrometer resolution (Fig. 1B and movie S1).

CTLs not only spread over the DAAM particles but also pushed into them, compressing the contact area into a synaptic "crater" ~10 µm in diameter (Fig. 1, B and C, and movie S1). As such, the CTL synapse contained two topographic zones: a peripheral "crater rim" dominated by positive curvature and an inner "crater floor" characterized by concave depressions. The crater floor was not smooth but rather micropatterned with discrete indentations, reliefs (hills), and ridges. To quantify the overall compressive strength of each synapse, we measured the deviation of DAAM particle shapes from an ideal sphere (Fig. 1, D and E, and fig. S1, A to C). This analysis confirmed that CTLs induced substantial particle compression within 5 min of establishing contact (Fig. 1F and movies S2 and S3). Although CTLs could maintain this mechanical configuration for substantially more than 30 min, the precise pattern of surface deformation was highly dynamic, as evidenced by the rapid decay of spatial autocorrelation within minutes (Fig. 1G). These dynamics were especially apparent at the crater floor, where F-actin-based protrusions induced a continuously changing deformation pattern (movies S1 to S3). Many of the topographical features in CTL-DAAM particle synapses were associated with F-actin-rich structures (Fig. 1C and movie S1), strongly suggesting that target deformation resulted from local cytoskeletal remodeling. Consistent with this interpretation, we found that latrunculin A (LatA), which inhibits actin polymerization, almost fully ablated target compression (fig. S2, A and B). To assess the effects of this drug on smaller distortions within the synapse, we enumerated convex reliefs and concave indentations using a watershedding approach (fig. S1, D to G). LatA treatment markedly reduced the number and magnitude of both feature types, further implicating F-actin in the act of target distortion (fig. S2, C to E). Collectively, these results indicate that CTLs use the F-actin cytoskeleton to form globally compressive synapses with dynamically undulating topography.

To determine whether CTLs form analogously shaped contacts with target cells, we imaged conjugates of perforin deficient  $(Prf1^{-/-})$  OT-1 CTLs and antigen-loaded B16 melanoma cells by confocal microscopy.  $Prf1^{-/-}$  CTLs were used to prevent the rapid cytoskeletal contraction and synapse dissolution induced by target cell apoptosis (32). The synapses that we observed were both dynamic and highly protrusive (Fig. 1H). CTLs physically displaced the surfaces of their targets, forming globally compressive, undulatory contacts that resembled the DAAM particle interactions (Fig. 1I). Quantification of target cell surface curvature values over time highlighted the close association between synapse formation and the development of

negative curvature, indicative of target compression (Fig. 1J and fig. S3). The architectural similarities between CTL-target cell and CTL-DAAM particle synapses strongly suggest that the DAAM particles capture physiologically relevant interfacial mechanics.

## CTLs release perforin and granzyme at the synaptic crater floor

Upon CTL target engagement, lytic granules containing perforin and granzyme traffic to the synapse, where they access the plasma membrane by moving through gaps in the cortical F-actin mesh (33–36). Exocytic fusion of these granules, a process termed degranulation, results in the directional release of perforin and granzyme into the intercellular space. Given that synaptic forces influence this process (26, 29), we sought to visualize degranulation concurrently with force exertion. OT-1 CTLs were transduced with a green fluorescent protein (GFP)–labeled form of the granule marker Lamp1 and then imaged with DAAM particles bearing anti-CD3ɛ and ICAM-1 (Fig. 2A). Close examination of granule dynamics revealed instances in which granules docked onto the synaptic membrane and then disappeared, indicative of exocytic fusion (Fig. 2, A and B, and movie S4).

To evaluate the local mechanical environment of these degranulation events, we generated a radially collapsed representation of each synapse topography by partitioning it into annular bins proceeding from the central zone outward, then graphed the distribution of surface curvatures in each of these bins as a function of distance from the contact center (Fig. 2, C to E). We also recorded the location and curvature at each degranulation position. We observed a strong preference for degranulation at the crater floor, within an intermediate band that excluded both the inner 20% and outer 20% of the synapse (Fig. 2E, blue lines). This pattern was notable given that the peripheral domain accounts for 36% of total contact area. In almost every case, the degree of curvature at a degranulation position hewed closely to the expected average curvatures at the corresponding radial location, implying that the degranulation machinery does not specifically target local convexities or local concavities. Instead, these results linked cytotoxic secretion to the undulatory crater floor as a whole, suggesting that the mechanical and architectural features of this subdomain potentiate cvtolvsis.

## Undulating topography maximizes cytotoxic efficiency in an in silico model

Prior studies indicate that synaptic forces promote killing by physically sensitizing the target cell membrane to perforin pore formation (26, 30, 37). Guided by our observation that degranulation occurs exclusively at the undulatory synaptic crater floor, we speculated that the mechanical features of this environment might allow CTLs to pair their chemical and physical outputs efficiently. To explore this idea, we developed a computational model based on continuum elastic theory to investigate the interplay between F-actin-based protrusive forces and target distortion. The synapse was simulated as a 10-μm region of CTL surface opposed to a deformable material representing the target particle (Fig. 3A). Simulations were performed at varying levels of synaptic F-actin coverage, and in each case, the effective free energy of the system was minimized to generate a snapshot of the CTL-target interface. The resulting topographies ranged from largely flat surfaces pockmarked with weak indentations to undulatory contours with pronounced hills and valleys (Fig. 3B). We

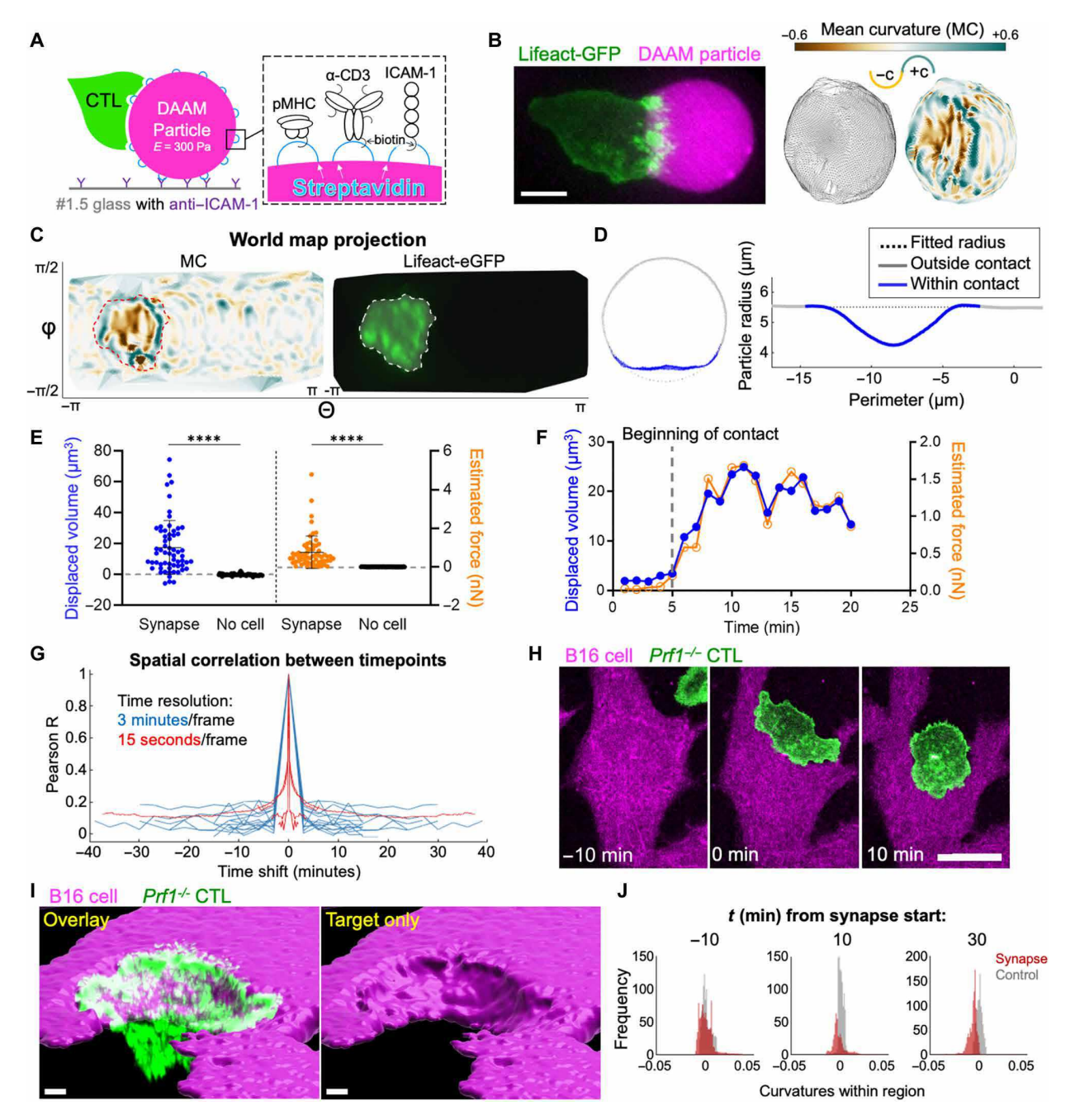


Fig. 1. CTLs form compressive, topographically complex synapses. (A) Schematic diagram of a T cell–hydrogel contact on glass (left) with DAAM-particle functionalization strategy (right). (B) Left, representative 3D projection of a Lifeact-eGFP expressing OT-1 CTL interacting with an H-2K<sup>b</sup>-OVA/ICAM-1–coated DAAM particle (magenta). Scale bar, 20 μm. Right, super-localized triangulations of the particle are shown, with triangles shaded blue-green for positive mean curvature and gold for negative mean curvature in the image at the far right. (C) Representative world map projection of the triangulated particle in (B), colored by mean curvature on the left, and by CTL Lifeact-eGFP intensity within 1 μm of the particle surface on the right. ROIs (dotted lines) were defined by the boundary of Lifeact-eGFP intensity. Θ and Φ denote polar coordinates in the world map view. (D) Left, cross section at the center of a representative CTL-bound particle, with contact area labeled in blue. Right, corresponding radial profile about the perimeter of the particle. (E) Integrated compressed volume (left) and estimated compression force (right) of CTL-DAAM particle contacts (n = 61) compared with unindented particles (n = 56). \*\*\*\* denotes  $P \le 0.0001$ , calculated by unpaired Welch's t test. Error bars indicate SD. (F) Particle distortion and force estimates over time from a representative time lapse in which contact is initiated at t≈5 min (see movie S2). Results in (E) and (F) are representative of at least three biological replicates. (G) Temporal autocorrelations of mean curvature profiles within the synapse ROI, determined from 19 time-lapse videos (three biological replicates). Blue traces were constructed from time-lapses with 3-min intervals, whereas red traces were constructed from 15 s/frame videos. (H to J)  $Prf1^{-/-}$  OT-1 CTLs expressing Lifeact-GFP were imaged together with antigen-loaded, CellTrace Yellow-labeled B16 cells. (H) Time-lapse montage of a representative contact. Scale bar, 15 μm. (J) Histogram

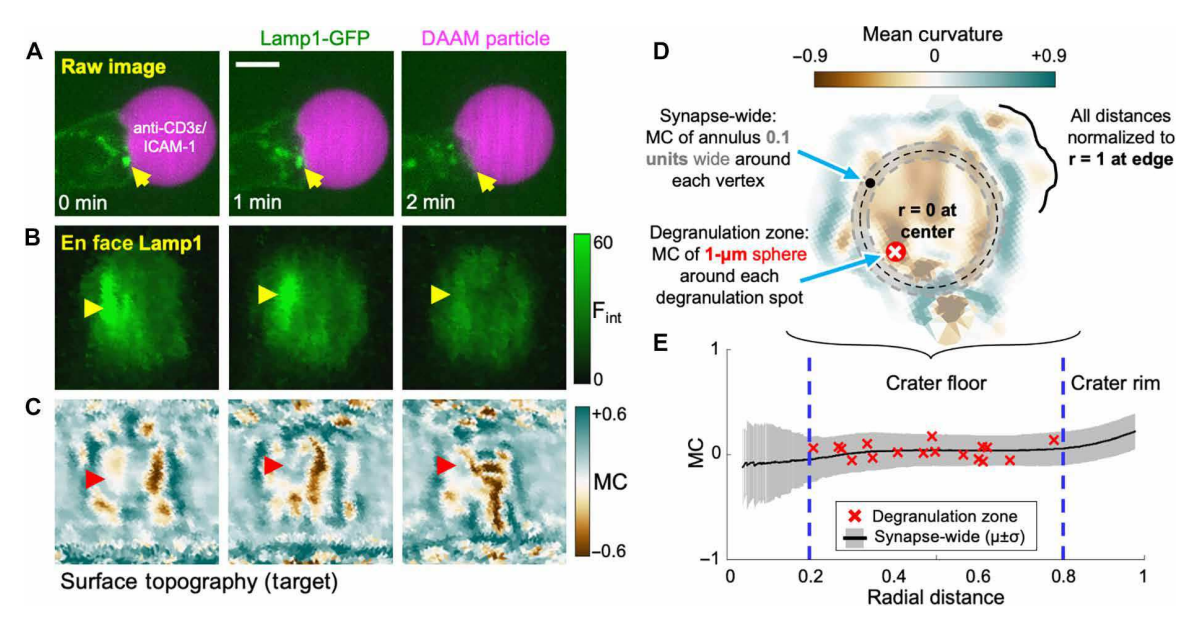


Fig. 2. Radial analysis of DAAM particle curvature and degranulation position. (A to C) Time-lapse montages of a representative Lamp1-eGFP expressing OT-1 CTL interacting with an anti-CD3ε/ICAM-1-coated DAAM particle. (A) Side view of the degranulation event. Scale bar, 5 μm. (B) En face view of Lamp1-eGFP within 0.5 μm of the particle surface. Yellow arrowheads denote a lytic granule that docks at the CTL-target interface and disappears, implying degranulation. (C) Cropped world map projection of the underlying particle surface, colored by mean curvature. The degranulation zone is indicated by red arrowheads. (**D** and **E**) The mean curvature in a 1-μm region centered on each degranulation event was compared with the mean curvature at that radial position within the synapse (see Materials and Methods). (D) Schematic of the analysis protocol. (E) Mean curvature (black line ± SD in gray) plotted as a function of normalized distance from the center of the contact. Mean curvatures around each degranulation event are plotted as red X's (n = 15 cells with n = 17 degranulation events, collected over two separate imaging sessions using CTLs derived from one mouse). Dotted blue lines indicate the inner and outer 20% of the synapse.

quantified the degree of deformation induced by protrusions in each simulation by calculating the increase in surface area and the variance of mean curvature across the 10-µm regions. Both metrics increased with F-actin coverage (Fig. 3C and fig. S4A), as expected. The organization of F-actin also mattered, however, with larger clusters inducing more pronounced distortion (Fig. 3C and fig. S4A).

Prior studies have shown that F-actin must be cleared from the synaptic membrane to enable lytic granule docking and exocytic secretion of perforin and granzymes (33-35). Accordingly, we explored the balance between exertion of F-actin-dependent forces at the synapse with the need to create F-actin-free sites for degranulation. We defined the area available for degranulation in each simulation as the total surface area situated at least 1 µm from the closest F-actin cluster; this "degranulatable area" increased with F-actin clustering across all F-actin coverages, reflecting how the consolidation of protrusive activity leaves more CTL membrane accessible to lytic granules (Fig. 3, D and E, and fig. S4B).

To better visualize the relationship between F-actin clustering and cytotoxic efficiency, we grouped simulations by F-actin cluster size and plotted them as contours in a 2D parameter space spanned by degranulatable area and target distortion. As expected, increasing cluster size shifted synapse contours upward and rightward (Fig. 3E and fig. S4B), indicative of increased efficiency. These gains, however, appeared to level off for F-actin clusters larger than ~1.2 µm in width (Fig. 3E and fig. S4B). This threshold cluster size mirrored that of real topographical indentations observed on DAAM particles (Fig. 3F), suggesting that F-actin features in this size range enable efficient combination of target distortion and degranulation. Similar limiting behavior was observed in simulations

where surface resistance parameters and granule size thresholds were varied (fig. S4C). At the saturating limits of these plots, any increase in target distortion or degranulatable area was offset by reductions in the other parameter. Tradeoffs of this kind are the defining feature of a Pareto frontier (38), a concept used in economics and engineering to describe the set of maximally efficient solutions to a multi-objective optimization problem. Our simulations suggest that F-actin protrusions of sufficient size enable CTLs to access their own set of maximally efficient cytolytic configurations.

Single-cell pattern analysis links undulatory synapse topography with cytotoxicity

We next investigated whether globally compressive, micropatterned synapse topography is a characteristic feature of cytotoxic potential by examining CTLs lacking critical regulators of F-actin-dependent force exertion (Fig. 4A). Our efforts focused on two actin nucleationpromoting factors: Wiskott Aldrich syndrome protein (WASp) and WASp-verpolin homology 2 (WAVE2). WASp generates mechanically active protrusions in the center of the synapse, whereas WAVE2 drives lamellipodial growth at the periphery (30). We also targeted talin, a scaffolding protein that couples integrins to the F-actin cortex and thereby enables force transmission through synaptic LFA-1 (39, 40). Previously, we had found that both talin and WASp are required for optimal in vitro cytotoxicity, whereas WAVE2 is dispensable (29, 30).

Talin, WASp, and WAVE2 were depleted from Cas9<sup>+</sup> OT-1 CTLs by retroviral transduction of sgRNA, and the resulting cells were mechanically profiled alongside control CTLs expressing nontargeting guides (sgNT). Fixed samples were used to facilitate comparison

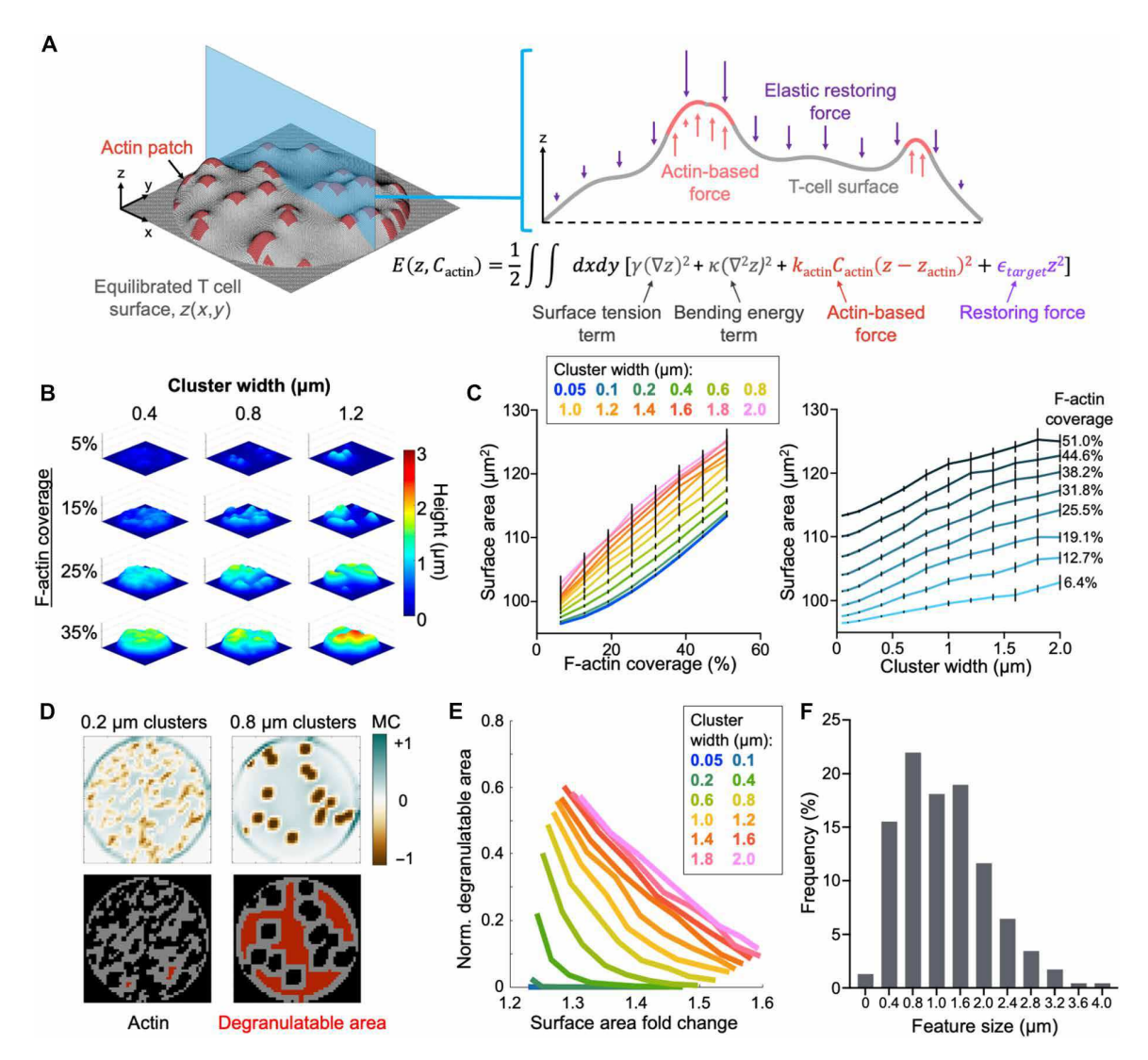


**Fig. 3.** In silico modeling of the cytolytic mechanotype. (**A**) In each simulation, protrusive F-actin clusters, modeled as spring-like harmonic potentials (orange), were opposed by membrane tension and bending rigidity (gray) in addition to restoring forces (purple) proportional to the elastic modulus of the deformable target. After placement of F-actin clusters in *x-y* space, energy minimization was performed and the resulting topography analyzed. (**B**) Representative simulation output over a range of F-actin coverage and cluster sizes. (**C**) Surface distortion, measured by total surface area, plotted as functions of F-actin coverage (left) and F-actin cluster size (right). Lines in the left graph indicate different cluster sizes, whereas lines in the right graph denote different degrees of F-actin coverage. Error bars denote SD, calculated from 10 replicate simulations. (**D**) Diagram highlighting the relationship between F-actin cluster size and degranulatable area, calculated using a 1-μm buffer. These simulations had equal levels of F-actin coverage. (**E**) Plot of surface distortion, measured by surface area change, graphed against degranulatable area. Each line encompasses the mean values of all simulations performed at the indicated F-actin cluster size over all F-actin coverage regimes. (**F**) Histogram showing the size distribution of concave synapse features, derived from P14 day 8 T<sub>eff</sub> cells (*n* = 68, representative of at least three biological replicates). For each measurement, the major and minor axes of the feature in question were averaged.

of hundreds of synapses 30 to 45 min after activation (Fig. 4B). Talin deficiency markedly weakened compressive strength (Fig. 4C) and protrusion formation (fig. S5A), whereas loss of both WASp and talin impaired the generation of convex reliefs within the synapse (fig. S5, B and C). By contrast, WAVE2-deficient CTLs exhibited none of these mechanical defects (Fig. 4C and fig. S5, A to C).

Although measurements of global compression and feature creation were useful for quantifying the overall magnitude of surface distortion, they failed to capture any information about the spatial patterning of topographical features within the synapse. To address this deficiency, we developed an alternative approach in which each

synapse topography was expressed as a linear combination of Zernike polynomials (41–43), a basis set of radial functions well suited for reconstructing roughly circular patterns (Fig. 4D). This process, which is similar to Fourier analysis, represents each surface curvature pattern as a spatial frequency spectrum (Fig. 4, D and E) defined by the weighting (modal) coefficients of constituent Zernike polynomials. We reasoned that spectra of this kind could be used to arrange topographies by similarity and expose the mechanical characteristics of cytotoxicity.

To apply this strategy to immune cell contacts, it was necessary to combine azimuthally related Zernike coefficients into a set of

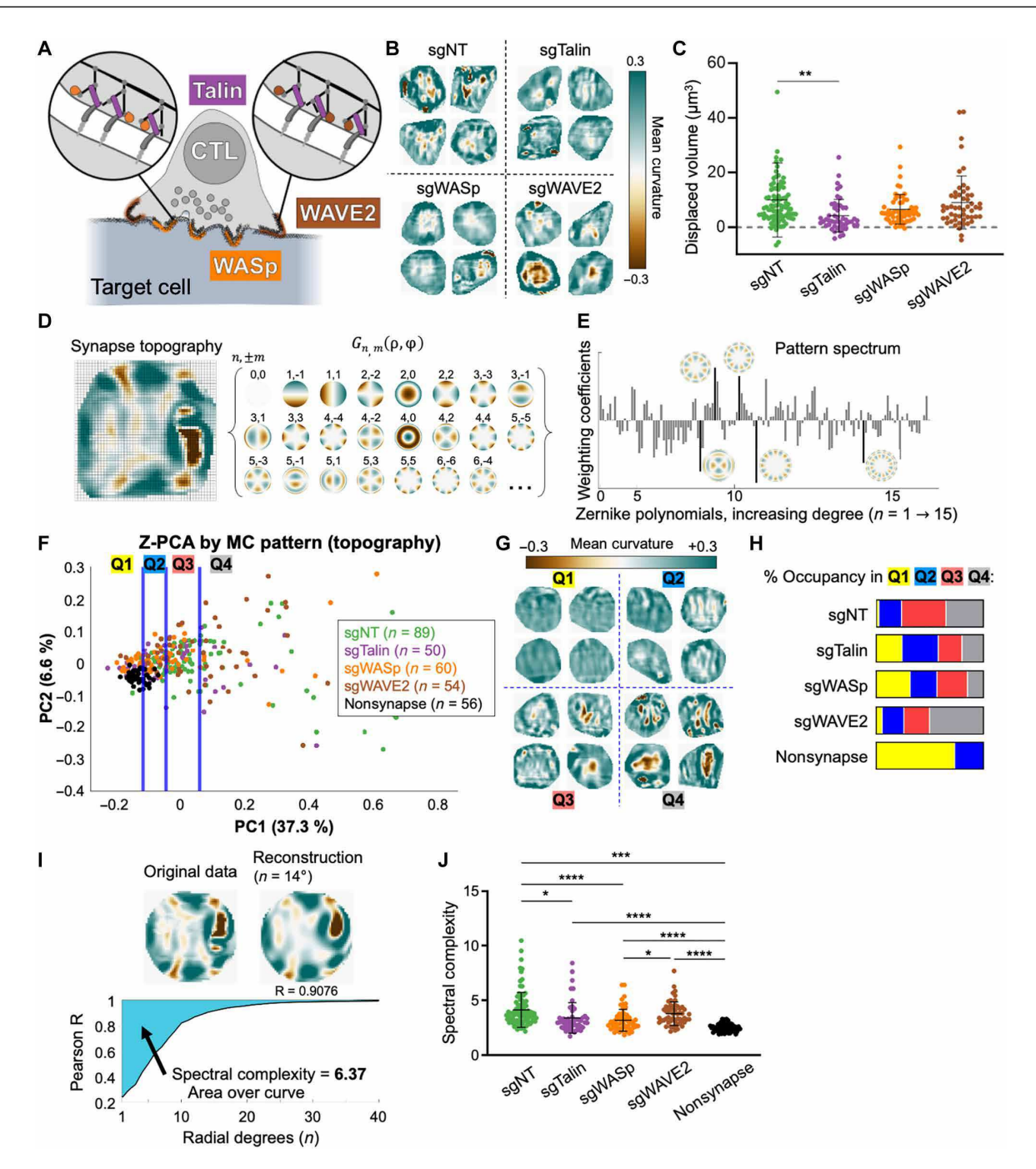


Fig. 4. Z-pattern spectral analysis links cytolytic activity to topographical complexity. (A) WASp and WAVE2 drive protrusive actin polymerization at the synapse, whereas talin couples integrins to the F-actin cytoskeleton. (B and D) OT-1 CTLs expressing Cas9 were transduced with retroviruses expressing the indicated sgRNAs or nontargeting control gRNA (sgNT) and then imaged together with DAAM particles coated with pMHC and ICAM-1. (B) Cropped views of representative synapses from each experimental group. (C) Deformation volume of CTL-DAAM particle contacts (n = 253 cells, representative of two biological replicates for sgNT, sgWAVE2, and sgWASp, and one biological replicate for sgTalin).\*\* denotes  $P \le 0.0021$ , calculated by multiple t test with Tukey's correction. Error bars denote SD. (D) Synapse topographies (curvature maps) were expressed as linear combinations of Zernike polynomials. Specific Zernike functions are classified by radial degree n and angular order m. (E) Zernike spectrum of the topography shown in (D). Bars represent the weighting coefficients for all Zernike modes in the first 15°. Representative functions are shown next to their corresponding bars, which are highlighted in black. (F) Topographies of the indicated CTL synapses, together with nonsynapse controls, were transformed into rotationally degenerate Z-pattern spectra and visualized by PCA. Data were separated into quartiles (divided by the blue lines) for downstream analysis. In this and all other Z-PCA plots, the fraction of sample variance explained by each principle component is expressed as a percentage. (G) Cropped views of representative synapse topographies from each quartile in (F). (H) Distribution of each experimental group across the PC1 quartiles. (I) For each topography of interest, its similarity (Pearson R) to its Zernike reconstruction was graphed as a function of Zernike degrees used in the reconstruction. Spectral complexity was defined as the area over this curve. (J) Spectral complexity metrics for the

rotationally degenerate indices that were insensitive to rigid-body rotation (fig. S6, A and B). Rotationally degenerate Zernike spectra of this kind were calculated for each CRISPR knockout and sgNT control synapse, along with topographies derived from unengaged DAAM particles. Zernike spectra (n = 314 total) were then arranged and visualized by principal components analysis (PCA) (Fig. 4F). Unperturbed surfaces ("nonsynapse") formed a tight, PC1-low cluster, whereas CTL topographies distributed to varying extents along PC1 and PC2 (fig. S6C). Binning the data into quartiles by the PC1 value (Fig. 4F, blue lines) highlighted the capacity of this approach to separate topographies into distinct pattern categories (Fig. 4G): Contacts in quartile 1 (Q1) were globally convex, reflecting the uncompressed state; Q2 comprised shallow craters with weak indentations; Q3 contained strong, finger-like protrusions; and Q4 comprised deep craters or claw-like contacts with sharp indentations. In general, features became stronger and more numerous as PC1 increased. Although wild-type and mutant CTLs were not neatly separated by this analysis, they distributed differently along the PC1 axis: Most control and WAVE2-deficient synapses occupied Q3 and Q4, whereas the majority of the WASp-deficient and talin-deficient contacts occupied Q1 and Q2 (Fig. 4H). CTLs with higher cytotoxic potential (control and WAVE2-deficient) also had larger mean values of PC1 (fig. S6, C and D), further linking this parameter with killing capacity. PC1 loadings comprised roughly equivalent contributions from a majority of low- and high-frequency Zernike modes, with the conspicuous exclusion of concentric functions (fig. S6E). We conclude that PC1, which accounts for a plurality (38.8%) of the pattern variation among topographies in this dataset, reflects both radial asymmetry and topographical complexity, suggesting that the capacity to induce complex, asymmetrical undulations on the target is a key feature distinguishing cytotoxic CTLs from killing-deficient mutants.

To test this hypothesis, we defined a spectral complexity index based on the rate at which Zernike reconstructions converge on a topography of interest (Fig. 4I). This metric is sensitive to local feature intensity and spatial variation: Uniformly strong or weak synapses both registered low spectral complexities relative to patterns in which concave and convex features alternate (fig. S7A). Spectral complexity correlated only weakly with particle compression at a singlecell level (fig. S7, B to G), indicating that the two metrics measure fundamentally distinct mechanical properties. By contrast, spectral complexity was strongly correlated with PC1 (fig. S6F), suggesting that it also captures radially asymmetric, undulating topography. Consistent with this interpretation, wild-type and WAVE2-deficient CTLs both exhibited higher spectral complexities than their WASpdeficient and talin-deficient counterparts (Fig. 4]). Collectively, these results establish a strong association between cytolytic potential and the induction of complex, asymmetric patterns on the target surface. Furthermore, they suggest that compressing the target surface into a crater and imposing undulating topography are two independent aspects of the CTL mechanotype, potentially regulated by distinct biochemical mechanisms.

CTLs lacking the lipid phosphatase PTEN are more cytotoxic in vitro and exert stronger F-actin-dependent synaptic forces (Fig. 5A) (26, 44). To evaluate the biophysical effects of this gain-of-function perturbation at high resolution, we mechanically profiled Cas9<sup>+</sup> OT-1 CTLs expressing an sgRNA against PTEN. PTEN-deficient CTLs killed antigen-loaded targets more avidly than sgNT controls (Fig. 5B), in agreement with prior work (26, 44), despite

lower levels of TCR-induced degranulation (Fig. 5C). In conjugates with stimulatory DAAM particles, PTEN-deficient CTLs formed deeper synaptic craters, indicative of stronger overall compression, and evoked more convex features on the target surface (Fig. 5, D and E, and fig. S8). sgNT and sgPTEN synapses formed overlapping distributions on Z-PCA plots (Fig. 5F), however, and they exhibited similar levels of spectral complexity (Fig. 5G). Thus, PTEN deficiency increases the strength of the cytolytic synapse without substantially altering its topographical organization. These results further support the idea that undulatory topography and compressive strength are independent components of the cytolytic mechanotype. They also indicate that our analytical approach can effectively identify qualitative and quantitative differences in mechanical output.

# Mechanical activity distinguishes CD8<sup>+</sup> CTL differentiation states during viral infection

Next, we investigated whether the mechanical indices that distinguish effective from incompetent CTLs in vitro would also delineate functionally distinct CD8+ T cell differentiation states generated in vivo. During an infection, naïve CD8<sup>+</sup> T (T<sub>n</sub>) cells differentiate into effector CTLs (Teff cells), which circulate and kill infected cells at sites of inflammation. A subset of Teff cells further differentiate into long-lived memory T (Tmem) cells (45), which have reduced cytolytic activity but can regenerate the T<sub>eff</sub> pool upon reinfection. In cases where CD8<sup>+</sup> T cells fail to clear the pathogen, chronic antigen exposure induces an "exhausted" (T<sub>exh</sub>) phenotype that is functionally hyporesponsive (46, 47). To mechanically profile these differentiation states, we used the lymphocytic choriomeningitis virus (LCMV) mouse infection model (48). The Armstrong LCMV strain induces an acute Teff response that clears the virus and then produces T<sub>mem</sub> cells, whereas the LCMV clone 13 strain establishes chronic infection that induces the formation of T<sub>exh</sub> cells. P14 T<sub>n</sub> cells, whose TCR recognizes the LCMV gp3333-41 antigen, were adoptively transferred into C57BL/6 mice, which were then infected with either Armstrong or clone 13 LCMV to yield T<sub>eff</sub> (8 days post-Armstrong), T<sub>mem</sub> (40 days post-Armstrong), and T<sub>exh</sub> (40 days post-Clone 13) cells on the same day (Fig. 6A). Differentiated T cell subsets and T<sub>n</sub> cells from uninfected P14 mice were sorted (fig. S9), incubated with anti-CD3ɛ/ICAM-1 DAAM particles, fixed, and imaged.

Volumetric analysis and feature identification revealed a hierarchy of compressive strength and protrusive activity, respectively, in the order:  $T_n < T_{\rm exh} \approx T_{\rm mem} < T_{\rm eff}$ .  $T_n$  cells formed the weakest compressions (Fig. 6B) and induced the shallowest curvature features (fig. S10, A and B), whereas  $T_{\rm eff}$  cells generated the strongest deformations, consistent with prior studies showing that  $T_{\rm eff}$  cells mount stronger and faster killing responses than the other subsets (49–52).  $T_{\rm mem}$  and  $T_{\rm exh}$  cells exerted intermediate levels of compression (Fig. 6B) but differed markedly in their capacity to create discrete indentations in the target surface, with  $T_{\rm exh}$  cells generating fewer protrusions than even  $T_n$  cells (fig. S10C). This result suggests that T cell exhaustion encompasses not only transcriptional and secretory responses (46, 47) but also biomechanical output.

Topographies from  $T_n$ ,  $T_{eff}$ ,  $T_{mem}$ , and  $T_{exh}$  subsets (n = 944 total) were subsequently subjected to Z-PCA analysis (Fig. 6C). Results were consistent with our prior experiments (Fig. 4 and fig. S6): Topographies spread as a continuum along a PC1 axis that excluded concentric Zernike functions (fig. S10D) and scaled with feature intensity and variation (Fig. 6D). Subset-specific differences became

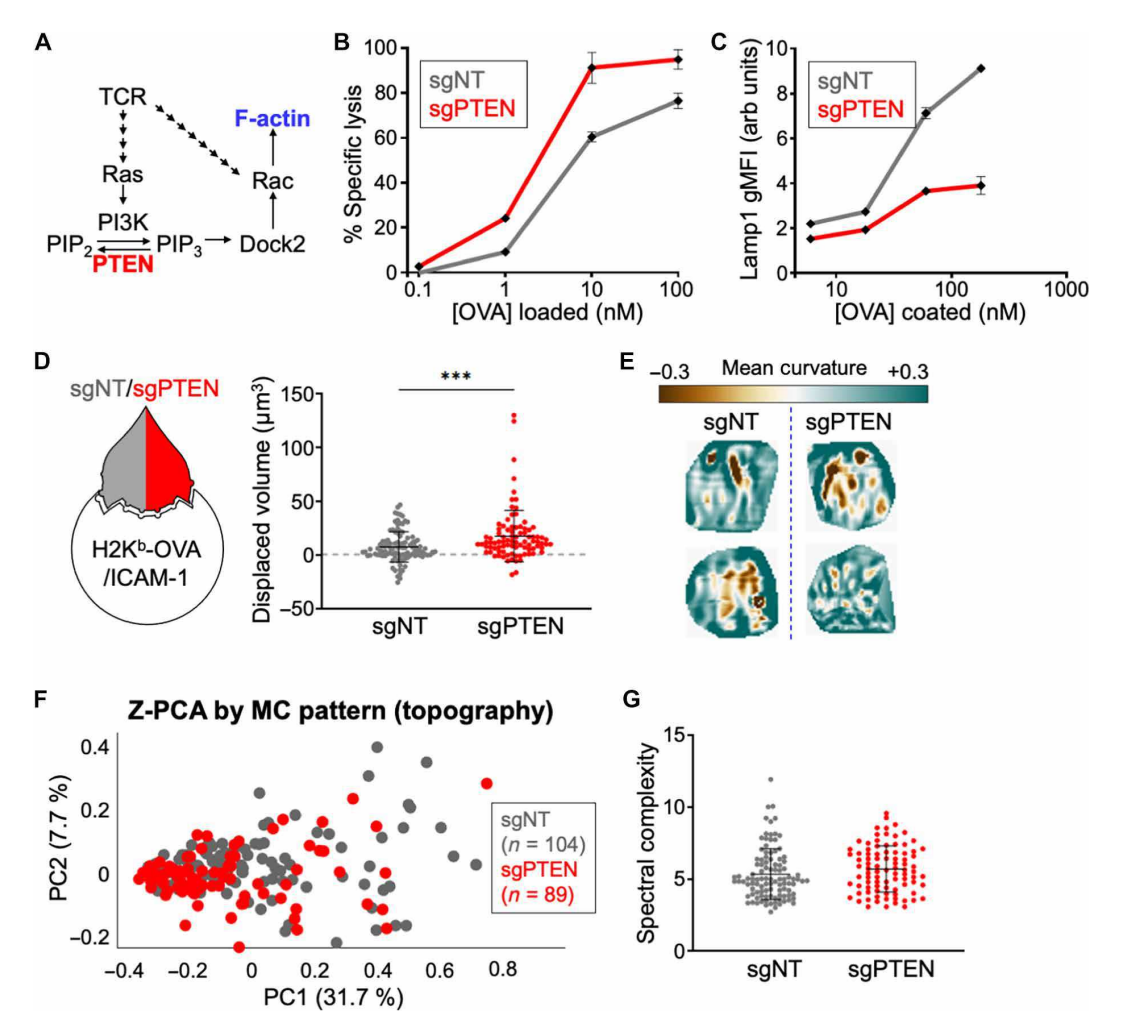


Fig. 5. PTEN deficiency boosts the compressive activity of the synapse. (A) P13K promotes synaptic F-actin and cytotoxicity via Dock2 (44). PTEN antagonizes this pathway. (B) Cytotoxicity of Cas9 $^+$  OT-1 CTLs transduced with sgPTEN or sgNT, measured using OVA-loaded EL4 target cells. Error bars denote SEM, determined from technical triplicates. Representative of at least two biological replicates. (C) sgPTEN or sgNT CTLs were mixed with H-2K $^b$ -OVA/ICAM-1-coated DAAM particles, and degranulation was assessed using surface exposure of Lamp1 by flow cytometry. Error bars denote SEM, determined from three biological replicates. (D to G) Cas9 $^+$  OT-1 CTLs transduced with sgPTEN or sgNT were imaged together with DAAM particles coated with pMHC and ICAM-1. (D) Deformation volume of CTL-DAAM particle contacts (n = 193 cells in total, pooled from three biological replicates). \*\*\* denotes  $P \le 0.0002$ , calculated by unpaired Welch's t test. Error bars denote SD. (E) Cropped views of representative synapses from each experimental group. (F) Synapse topographies were transformed into Zernike spectra and then visualized by PCA. (G) Spectral complexity of the indicated CTL synapses, with error bars indicating SD.

particularly evident after partitioning the Z-PCA plot into PC1quartiles: The vast majority of T<sub>n</sub> cells occupied the PC1-low regions Q1-2, whereas most T<sub>eff</sub> cells fell into the PC1-high Q4 region (Fig. 6E). T<sub>mem</sub> cells displayed an intermediate distribution that spread between Q2-4, whereas most Texh cells straddled Q1-3. The leftward PC1 shift of T<sub>exh</sub> cells relative to their T<sub>mem</sub> counterparts further supports the idea that the former are mechanically hypofunctional. In agreement, T<sub>eff</sub> cells exhibited the highest spectral complexities, followed by  $T_{mem} > T_{exh} > T_n$  (Fig. 6F). Although this ordinal trend in spectral complexity resembled that of compressive strength, the two parameters again did not correlate on a single-cell level (fig. S10, E to I). We conclude that the capacity to create complex, undulatory surface patterns within the compressive synaptic crater distinguishes cytotoxic T<sub>eff</sub> cells from noncytotoxic (T<sub>n</sub>) and weakly cytotoxic (T<sub>mem</sub> and T<sub>exh</sub>) cells, suggesting that this mechanotype potentiates cytolytic function in vivo.

# Cytotoxic synapsis is mechanically distinct from nonlytic synapsis and phagocytosis

Having distinguished the mechanotype of killing-competent CTLs in two different contexts, we examined the relationship between interfacial mechanics and cellular ontogeny more broadly. We initially compared two functionally distinct  $T_{\rm eff}$  cell subsets: CD8<sup>+</sup> OT-1 CTLs versus CD4<sup>+</sup> helper T ( $T_{\rm HC}$ ) cells expressing the class II MHC–restricted 5C.C7 TCR. Measurements were performed using anti-CD3e/ICAM-1–coated DAAM particles to circumvent potential artifacts arising from differential TCR-pMHC binding affinities (fig. S11A).  $T_{\rm HC}$  cells formed crater-like contacts that were similar to CTL synapses in their overall structure (convex rim, concave floor). CTLs imparted significantly stronger compressive forces (fig. S11B), however, along with sharper, more numerous indentations (fig. S11, C and D) and reliefs (fig. S11E). In a Z-PCA analysis (n = 548 total), CTL and  $T_{\rm HC}$  cell topographies spread along a PC1

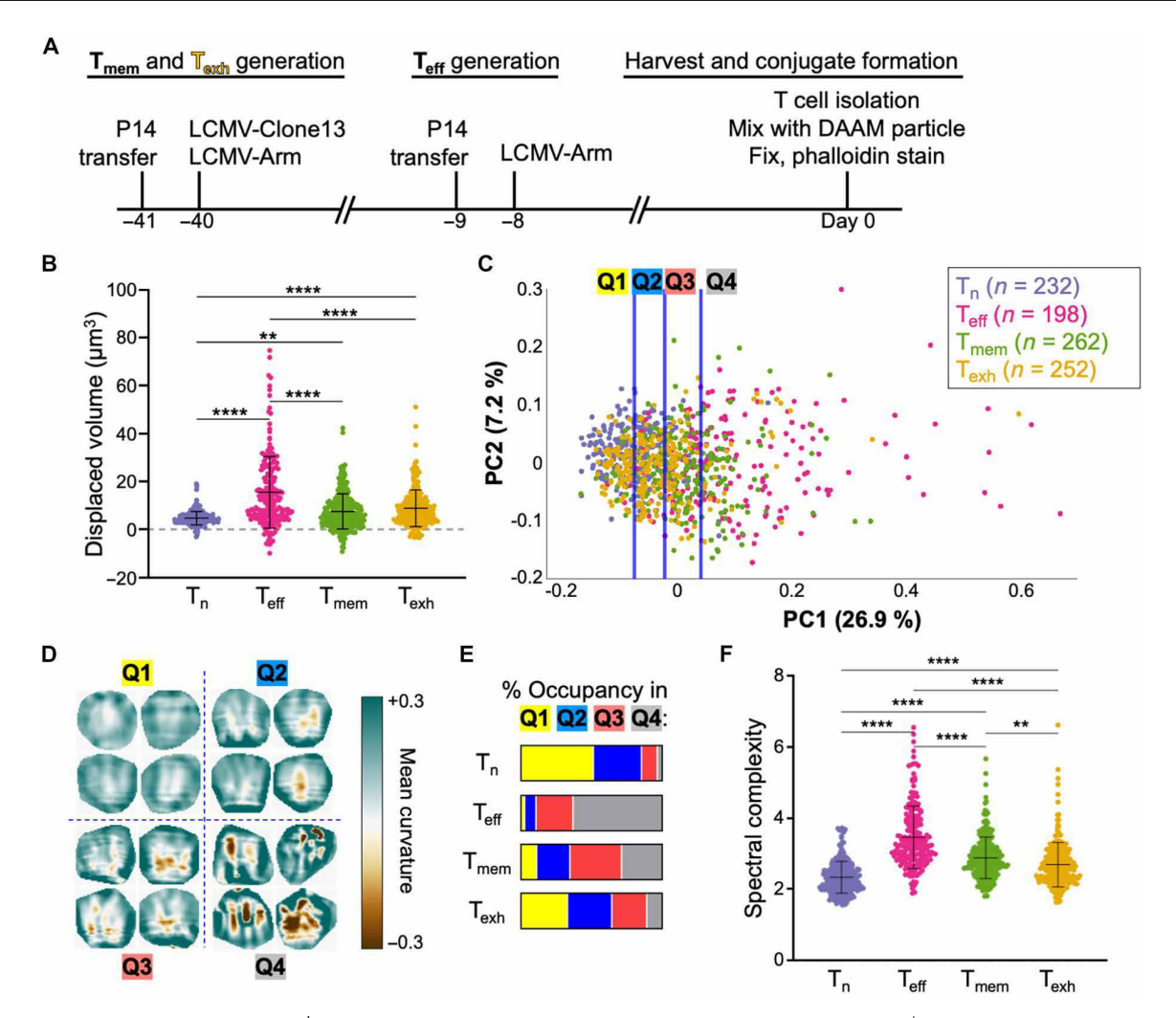


Fig. 6. Mechanical activity distinguishes CD8<sup>+</sup> T cell differentiation states. (A) Protocol for in vivo differentiation of CD8<sup>+</sup>  $T_{mem}$ ,  $T_{exh}$ , and  $T_{eff}$  cells expressing the P14 TCR. All three cell types, together with  $T_n$  P14T cells, were isolated concurrently and imaged together with DAAM particles coated with anti-CD3 $\epsilon$  and ICAM-1. (B) Deformation volume generated by each T cell subset (n = 944 in total, pooled from three biological replicates). \*\* and \*\*\*\* denote  $P \le 0.0021$  and  $P \le 0.0001$ , respectively, calculated by multiple t test with Tukey's correction. Error bars denote SD. (C) Synapse topographies were transformed into Zernike spectra and then visualized by PCA. Data points were separated into quartiles (divided by the blue lines) for downstream analysis. (D) Cropped views of representative synapses from each quartile in (C). (E) Distribution of each P14 subset across the quartiles of PC space. (F) Spectral complexity metrics for all P14 subsets. \*\* and \*\*\*\* denote  $P \le 0.0021$  and  $P \le 0.0001$ , respectively, calculated by permutation testing with Benjamini-Hochberg correction for multiple hypothesis testing. Error bars denote SD.

axis that again represented complexity and radial asymmetry (fig. S11, F and G). Lytic and nonlytic topographies were present in all parts of this plot (fig. S11H), implying that both cell types can induce strong, complex topographies. However, we found that almost half of the  $T_{\rm H}C$  cell synapses fell into the PC1-low region (region T1), whereas only a quarter of CTL contacts did so (fig. S11I). CTL synapses also exhibited significantly higher spectral complexity values (fig. S11J), indicating that CTLs impart stronger and more complex distortion patterns than  $T_{\rm H}C$  cells. This further substantiates the link between cytolytic activity and topographical complexity.

That every T cell subset we investigated formed compressive contacts led us to ask whether this configuration was a bona fide feature of T cell synapsis or merely the inevitable result of cell spreading on a soft, spherical particle. To address this issue, we examined the mechanical output pattern of phagocytosis, a process that has been likened to synapse formation because of some shared

signaling pathways, cytoskeletal features, and organelle polarization events (53, 54). The functional end points of these two processes are very different, however, implying that they might be mechanically distinguishable (20). We therefore imaged fixed bone marrow–derived macrophages (BMDMs) engulfing immunoglobulin G (IgG)–coated DAAM particles and compared them with fixed preparations of OT-1 CTLs bound to anti-CD3ɛ/ICAM-1–coated targets (Fig. 7A).

BMDM contacts were globally tensile, pulling at the center of the phagocytic cup while pinching along the periphery (Fig. 7, B and C). This pattern of mechanical activity was essentially opposite to the global compression seen in T cell synapses (Fig. 7D). We plotted the mean curvature distributions of each type of contact in radial shells proceeding from the center of the interface to the periphery (fig. S12, A to C), then determined the difference in these distortion maps to identify mechanical activities enriched in CTLs or BMDMs

(Fig. 7E). Whereas CTL plots sloped upward (blue), indicative of cratering and compression, BMDM plots sloped downward (red), reflecting central tugging and peripheral squeezing. BMDMs formed deeper and more numerous protrusions than CTLs (Fig. 7, F to H), but they appeared to organize these structures in a different way. In some cases, protrusions dotted the periphery of the phagocytic cup, akin to the tooth-like actomyosin structures shown recently to mediate lateral pinching of targets (22, 55). In other instances, protrusions were evoked closer to the center of the contact without altering the convex tone of this region (Fig. 7B). Collectively, these results indicate that phagocytosis and synapsis use fundamentally distinct forms of interfacial mechanics.

Z-PCA cleanly separated phagocytic cups from CTL synapses (Fig. 7I). Again, PC1 contained contributions from most Zernike modes but excluded key concentric functions, indicative

of complexity and radial asymmetry (fig. S12D). Accordingly, strongly undulating topographies occupied PC1-high regions, whereas interactions with more muted curvature variation were PC1 low. By contrast, PC2 segregated CTL synapses, which were overwhelmingly PC2 high, from the largely PC2-low BMDM contacts. PC2 loadings included sizable contributions from two low-order, concentric Zernike modes reflecting global convexity (4,0) and concavity (2,0) (fig. S12D), which together distinguished compressive synapses from tensile phagocytic cups. These results demonstrate that, in contrast with T cell synapsis, BMDMs strongly manipulate their targets within a globally tensile configuration that accentuates cargo convexity. The marked differences between these two mechanotypes suggest that they do not result inevitably from close contact and adhesion, but rather reflect cellular intent.

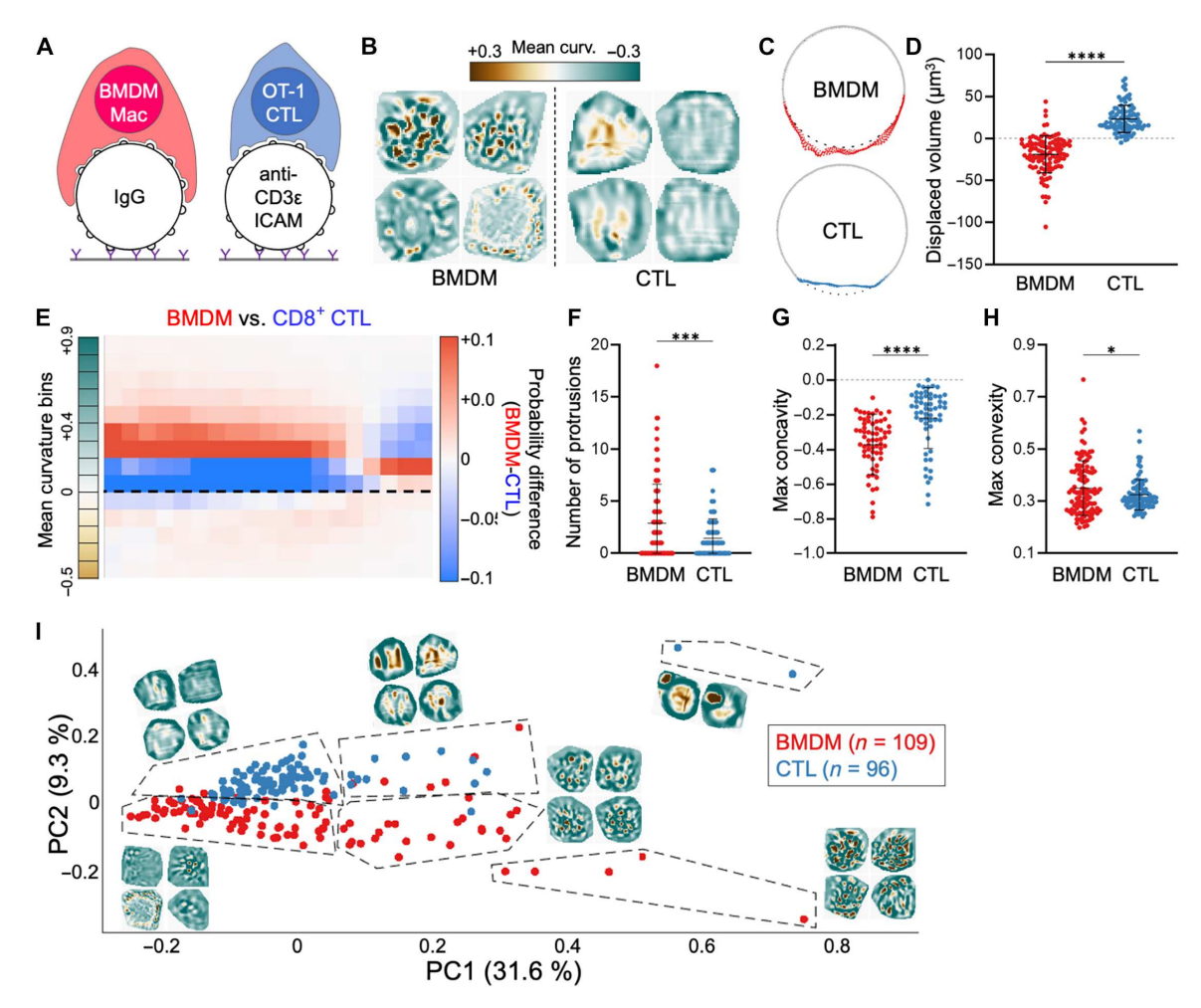


**Fig. 7. Macrophages and T cells use inverse interfacial mechanotypes.** (**A**) OT-1 CTLs and C57BL/6 BMDMs were cultured in parallel and imaged together with anti-CD3 $\epsilon$ /ICAM-1–coated and IgG-coated DAAM particles, respectively. (**B**) Cropped views of representative BMDM and CTL contacts, colored for curvature. (**C**) Cross-sectional view of representative BMDM and CTL contacts, with contact areas colored red asnd blue, respectively. Dotted lines indicate the footprint of an unperturbed sphere. (**D**) Deformation volume of BMDM (n = 109) and CTL (n = 96) contacts. Representative of two biological replicates. (**E**) Difference plot of radial curvature distribution, determined by subtracting the CTL and BMDM curvature distributions from each other. Curvature domains are colored red and blue for overrepresentation ( $\Delta$  probability density) of BMDMs and CTLs, respectively. Dotted line indicates 0 curvature (flat). (F to H) Quantification of protrusion number (**F**), peak indentation concavity (**G**), and peak relief convexity (**H**) within BMDM and CTL contacts. (**I**) Z-PCA of BMDM and CTL topographies. Representative topographies from each Z-PCA region have been overlaid onto the plot. In (D) and (F) to (H), \*, \*\*\*, and \*\*\*\* denote  $P \le 0.0332$ ,  $P \le 0.0002$ , and  $P \le 0.0001$ , respectively, calculated by unpaired Welch's t test. All error bars denote SD.

### Cytolytic synapse architecture is adaptive

Last, we investigated whether CTLs adapt their synaptic architecture and mechanics to the physical properties of their targets by comparing contacts formed by OT-1 CTLs on soft (300 Pa) and stiff (3000 Pa) DAAM particles coated with pMHC and ICAM-1 (Fig. 8A). We included both wild-type (sgNT) and PTEN-deficient (sgPTEN) CTLs in this analysis, reasoning that the enhanced mechanical capacity of sgPTEN CTLs might affect their response to target rigidity. Both groups of CTLs largely failed to distort the stiff particles (fig. S13A), demonstrating that a 10-fold increase in target rigidity profoundly alters the mechanical outcome of synapse formation.

Next, we asked whether increased rigidity affects the mechanical strategy used by CTLs for target engagement by assessing synaptic F-actin architecture as an index of cellular deformation strategy. CTLs used an assortment of interfacial F-actin configurations, ranging from multifocal contacts with numerous discrete puncta to confluent sheets with only subtle variations in fluorescence intensity (Fig. 8B). To parse this diversity, we performed Z-PCA analysis using the phalloidin signal as input (Fig. 8C). Synapses were spread along a PC1 axis containing large contributions from two loworder concentric Zernike functions, (2,0) and (4,0) (Fig. 8, C and D). This loading combination is expected to capture annularity, or enrichment at the periphery of the contact relative to the center. Accordingly, almost all synapses with positive PC1 (region T3 in Fig. 8E) contained peripheral F-actin rings, whereas synapses with negative PC1 (region T1) exhibited smooth F-actin distributions,

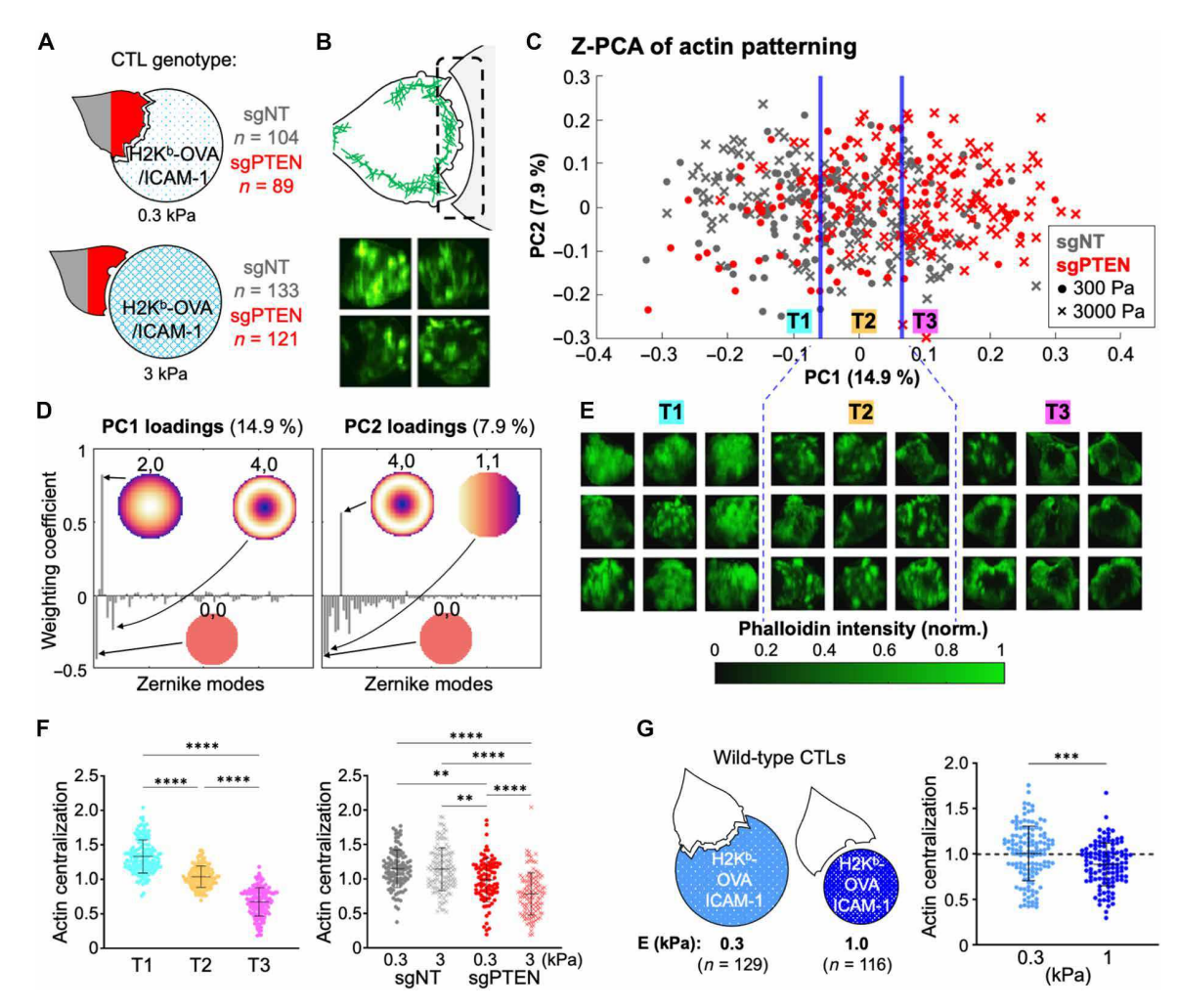


**Fig. 8. The cytolytic mechanotype is adaptive.** (**A** to **F**) Cas9<sup>+</sup> OT-1 CTLs transduced with sgPTEN or sgNT were mixed with 13-μm-diameter 300- or 3000-Pa pMHC/ICAM-1-coated DAAM particles, fixed, phalloidin-stained, and imaged. (**B**) En face synaptic F-actin images were captured by extracting the integrated F-actin fluorescence signals 0.5 μm from the particle surface. (**C**) Z-PCA analysis of sgPTEN and sgNT F-actin patterns on 300- and 3000-Pa particles. Data points were separated into terciles (divided by the blue lines) for downstream analysis. n = 447 total, pooled from three biological replicates. (**D**) Zernike polynomial loading for PC1 (left) and PC2 (right). Major contributing modes are indicated. (**E**) Cropped views of representative synapses from each quartile in (C). (**F**) Actin centralization, determined by dividing the phalloidin MFI in the central domain of the synapse with the phalloidin MFI in the peripheral domain (see Materials and Methods), plotted by Z-PCA tercile (left) and experimental group (right). \*\* and \*\*\*\* denote  $P \le 0.0332$  and  $P \le 0.0001$ , respectively, calculated by multiple t test with Tukey's correction. (**G**) OT-1 CTLs were mixed with 300-Pa, 13-μm (n = 129) or 1000-Pa, 9-μm DAAM (n = 116) particles coated with pMHC/ICAM-1, fixed, phalloidin-stained, and imaged. Graph to the right shows actin centralization for each experimental group. n = 245 total, pooled from three biological replicates. \*\*\* denotes  $P \le 0.0002$ , calculated by unpaired Welch's t test. All error bars denote SD.

and synapses with PC1  $\sim$  0 (region T2) were predominantly multifocal. To measure annularity directly, we defined "F-actin centralization" as the ratio of mean F-actin fluorescence intensity in the center of the contact to that of the peripheral rim. T3 contacts were the least centralized (most annular) by this measure, followed by those in T2 and then T1 (Fig. 8F). Neither particle compression nor topographical complexity correlated with F-actin centralization at the level of individual synapses (fig. S13B).

A majority of sgPTEN synapses on stiff targets were situated in T3, whereas most sgPTEN contacts on soft particles and both sgNT samples occupied the T1 and T2 regions (Fig. 8C and fig. S13C). This difference in pattern distribution suggested that stiff sgPTEN synapses exhibit more annular F-actin, an assessment we confirmed by measuring F-actin centralization (Fig. 8F). These data indicated that sgPTEN cells can adapt their synaptic F-actin configuration in response to target rigidity. Because PTEN deficiency is known to increase synapse size (44), we speculated that using smaller targets might enable us to trigger analogous stiffness-dependent F-actin reorganization in wild-type CTLs. To this end, we prepared stiffer, smaller DAAM particles (1000 Pa, 9-µm diameter) coated with pMHC and ICAM-1. These targets elicited significantly more ringlike F-actin from wild-type CTLs than did soft particles of standard diameter (300 Pa, 13 µm) (Fig. 8G). These results demonstrate not only that the cytotoxic mechanotype is mechanosensitive but also that PI3K signaling influences the adaptive thresholds that control this behavior.

#### **DISCUSSION**

Although immune cell-cell interactions both sense and impart mechanical forces, precisely how these forces are organized and the extent to which this organization controls immune function remain poorly understood. To address these issues, we developed a highresolution approach for profiling the mechanical output of immune cells and identifying critical features that delineate functionally distinct leukocyte subsets. Instrumental to our efforts was the application of spectral analysis to compare thousands of single-cell force exertion patterns. In this manner, we demonstrated that macrophage phagocytosis and T cell synapsis exhibit inverse patterns of pushing and pulling. We also found that T cell cytotoxicity is closely associated with the capacity to distort target surfaces into compressive synaptic craters containing complex undulations. This mechanotype correlated with cytolytic potential across multiple cell type comparisons. Together, our results indicate that the precise mechanical disposition of an immune cell-cell interaction reflects its specific function and that interfacial mechanotypes can be used to distinguish immune subsets.

Three lines of evidence suggest that the cytotoxic mechanotype we have characterized is required for optimal killing. First, formation of a topographically complex synaptic crater was closely associated with lytic potential among disparate CTL differentiation states and in comparisons of cytotoxic and noncytotoxic T cells. Second, degranulation localized exclusively to the inner floor of the synaptic crater, close to the undulatory surface of the target. Third, computational modeling strongly suggested that this mechanical output pattern enables CTLs to maximize killing efficiency. Collectively, these results are consistent with imaging-based studies of degranulation position (33–35, 37, 56) and with prior work implicating synaptic force exertion in the potentiation of perforin activity (26, 30). Perforin was

recently shown to preferentially bind to and oligomerize in convex membranes, presumably because gaps between phospholipids in the outer leaflet of a curved bilayer encourage interdigitation by hydrophobic proteins (37). Given this predilection of perforin for membrane convexity, it is noteworthy that CTLs do not degranulate at the peripheral rim of the synapse, which is highly enriched in positive curvature. We speculate that any gains in cytotoxic potency realized by releasing perforin at the rim would be offset by the risks of leaking this toxic protein out of the synapse, where it could damage innocent bystander cells. CTLs instead secrete perforin and granzyme at the undulatory synaptic crater floor. Although this domain is predominantly negative in curvature, its complex topography generates multiple focused convexities. Because local curvature and, by extension, curvature-induced packing defects, should increase with decreasing membrane area (57), we expect that these focused convexities will be strongly sensitized to perforin, more so than a synaptic membrane with global, uniform positive curvature. Hence, by degranulating close to microscale distortions in the center of the synapse, CTLs could potentiate their killing responses without sacrificing host security.

In silico modeling of F-actin-based force exertion against a deformable target enabled us to generate synapse topographies that grossly resembled our experimental observations and revealed key insights about killing efficiency. One such insight is that consolidating protrusive F-actin into clusters increases target distortion per unit of F-actin while simultaneously leaving more plasma membrane free for degranulation. This win-win relationship could be a key evolutionary driver underlying the development of the cytotoxic mechanotype. We also found that the marginal benefits of additional clustering diminish beyond a cluster width of ~1 μm, implying that there is little need to build larger structures within the crater floor to potentiate killing. Last, we identified a Pareto frontier in plots of cytotoxic efficiency that encompasses the set of all "maximally efficient" mixtures of F-actin coverage and degranulatable area. The existence of multiple comparably efficient synaptic states is intriguing given that the molecular composition of a CTL, in particular its cytotoxic proteins, can fluctuate widely on the basis of its differentiation state and recent killing history (49, 58, 59). It is tempting to speculate that a CTL might select the Pareto-efficient mechanotype that most effectively exploits its current cytolytic and cytoskeletal capacities.

That  $T_{\rm exh}$  cells used a weaker and less undulatory mechanotype than  $T_{\rm mem}$  cells suggests that defective mechanical output is an integral part of the exhaustion program. The basis for this lack of strength remains to be identified, but transcriptomic studies of T cell exhaustion have documented widespread changes in gene expression that affect both the composition of the cytoskeleton and the metabolic pathways that fuel its remodeling (58, 60). F-actin dynamics are particularly costly from an energetic standpoint, accounting for half of cellular adenosine 5'-triphosphate consumption (61, 62); attenuating these dynamics could enable  $T_{\rm exh}$  cells to survive in nutritionally restricted contexts like the tumor microenvironment.

Although T cell synapses were globally compressive, macrophage contacts adopted a tensile configuration consistent with engulfment. Mechanistically, the microparticle distention we observed toward the base of phagocytic cups could be caused by direct pulling at the center of the contact or by lateral squeezing of the targets leading to elastic bulging into the central domain. Further studies are needed to distinguish between these possibilities, which are not mutually

exclusive. What our results make evident, however, is that the compressive mechanotype exhibited by T cells is not the inevitable consequence of building an F-actin-based interface on a deformable surface. Rather, the interfacial mechanotype applied by an immune cell of interest is likely a function of multiple factors, including cell size, actin availability, cellular energy status, cytoskeletal composition, the amplitude and spatial disposition of signaling, and the relative rigidities of the immune cell and its partner.

Using DAAM particles of different size and rigidity, we found that CTLs shift their synaptic F-actin configuration to a more ring-like pattern on stiffer, smaller targets. Although the purpose of this architectural transition remains unclear, the fact that both annular and nonannular F-actin patterns impose similar levels of compression and complexity implies that CTLs can use multiple biomechanical strategies to distort the target surface. An annular contact could, for example, generate undulatory topography through some combination of tangential stretching and central folding, ultimately achieving a similar degree of deformation as a group of discrete synaptic protrusions. Prior studies have suggested that macrophages modulate their phagocytic uptake strategy to match the mechanical properties of their cargo (19, 22, 63, 64). Our present results indicate that cytotoxic lymphocytes modulate their killing responses in an analogous fashion.

Although there have been prior efforts to apply Zernike polynomials to biological images (65), the utility of this approach has been limited by the fact that Zernike modes have a fixed angular orientation. Consequently, the spectralization process interprets patterns related by simple rotations to be fundamentally distinct. Combining coefficients into a rotationally degenerate representation enabled us to circumvent this problem and effectively compare complex synapse topographies and F-actin patterns lacking an intrinsic radial orientation. This strategy should be applicable to any dataset containing images of roughly circular dimensions. Moving forward, we expect that the thoughtful pairing of orthogonal basis sets (e.g., Zernike polynomials) with appropriate data types will find broad applicability in the analysis of cellular patterning. As imaging datasets become larger and more complex, methods for interpreting complexity and parsing heterogeneity will be critical for extracting meaningful biological information. Spectral decomposition represents an alternative and complementary approach to algorithms based on a supervised classifier (66), and although both strategies cluster data in an unbiased manner, spectralization coupled with PCA has the advantage of generating interpretable axes of separation, thereby providing more potential mechanistic insight.

Together, the mechanical observables we have defined in this study comprise a toolkit for illuminating the enigmatic biophysical dimension of immune cell activity. Deciphering the molecular principles underlying interfacial mechanotypes could unlock the mechanical logic of immune cell-cell interactions and generate new avenues for selective modulation of these contacts in both homeostatic and pathological conditions.

#### **MATERIALS AND METHODS**

#### Study design

The goal of this study was to determine the biomechanical signature of lymphocyte cytotoxicity. To this end, we used super-resolution fluorescence microscopy to image murine CTLs in contact with stimulatory DAAM particles. CRISPR-Cas9 technology was used to knock out specific genes, and the effector activities of various modified CTLs were assessed using functional in vitro assays. Last, we applied in silico simulation methods to explore the relationship between synapse topography and cytotoxic efficiency. Experimental sample sizes were not predetermined, and there were no predefined study end points. Experiments were not randomized, and investigators were not blinded during data acquisition and analysis. In general, experiments were performed at least twice (two biological replicates). Specific information about replication is included in the figure captions. Data analysis protocols are detailed below and in the Supplementary Materials.

### DAAM particle functionalization

DAAM particles were first streptavidinylated using amine coupling as previously described (20): Briefly,  $4.0 \times 10^7$  beads were activated with 1-ethyl-3-(3-dimethylaminopropyl)carbodiimide [Thermo Fisher Scientific (TFS) 22980] and N-hydroxysuccinimide (NHS; TFS 24500) in MES buffer (pH 6.0) with 0.1% (v/v) Tween 20. Then, the buffer was exchanged into basic phosphate-buffered saline (PBS; pH 8.0) with 0.1% Tween 20 for a 2-hour conjugation with 12 μM streptavidin (Prozyme, SA10) and 100 μM fluorescent dye (Alexa Fluor 488 Cadaverine or Lissamine Rhodamine B ethylenediamine, TFS A30676 or L2424, respectively). Unreacted carboxy-NHS was quenched with excess ethanolamine for 30 min, and the resulting DAAM particles were exchanged into PBS (pH 7.4). For T cell experiments, batches of  $5.0 \times 10^6$  fluorescent streptavidinylated DAAM particles were incubated for 2 hours in 1 ml of PBS containing 500 nM tail-biotinylated ICAM-1 (residues 28 to 485) and 7.5 nM of either (i) tail-biotinylated cognate pMHC complex or (ii) biotinylated Armenian hamster anti-CD3ɛ antibody (clone 145-2C11, Bio-Legend 100304). ICAM-1 and pMHC proteins were expressed and purified as described (29). For macrophage experiments, batches of  $5.0 \times 10^6$  fluorescent streptavidinylated DAAM particles were incubated with 500 nM biotinylated mouse IgG (Jackson Immunoresearch 015-000-003). After all coatings, beads were washed >3 times by centrifugation at 12,000g, resuspended in clean PBS, and then used for imaging experiments within 3 days.

Imaging of cell-particle conjugates
For T cell assays, 2 × 10<sup>5</sup> ICAM-1<sup>+</sup> beads were adhered overnight onto 170-µm imaging coverslips (Ibidi µ-Slide 8 Well, #80826) coat-

onto 170-μm imaging coverslips (Ibidi μ-Slide 8 Well, #80826) coated with biotin-poly-L-lysine, blocked with 0.5% (m/v) bovine serum albumin in PBS, coated with streptavidin (10 μg/ml) in blocking buffer, and then coated with biotinylated rat anti-ICAM-1 antibody (1 μg/ml; clone YN1/1.7.4, eBioscience, TFS 13-0541-85). Biotinpoly-L-lysine was produced by incubating poly-L-lysine hydrobromide (5 mg/ml; Sigma-Aldrich P6282) with 1.5 mM EZ-Link Sulfo-NHS-biotin (TFS 21217) in basic phosphate buffer, followed by quenching with excess glycine. Before addition of T cells, DAAM particles were exchanged into complete RPMI by a series of well dilutions, taking great care to keep the particles submerged in fluid throughout. For fixed experiments, 1 to  $1.2 \times 10^5$  T cells were pipetted into each well and left for 30 to 45 min (37°C and 5.0% CO<sub>2</sub>) to form synapses. Afterward, they were fixed with prewarmed 4% (v/v) paraformaldehyde (PFA) in PBS, incubated for 15 min, and washed. For macrophage experiments, 5 to  $7.5 \times 10^4$  day-7 cultured macrophages were deposited onto eight-well chambers directly and left to attach and acclimatize overnight. The next day, 0.5 to  $1.0 \times 10^5$  IgGcoated particles were deposited into the wells, and conjugates were PFA-fixed after <15 min as described above. To fluorescently stain cellular F-actin, conjugates were first permeabilized using PBS with 0.1% (v/v) Triton X-100 (PBSTx). Wells were blocked using PBSTx with 1% (m/v) goat serum for 1 hour, then stained using this buffer with 165 nM Alexa Fluor 488 or 568 phalloidin (TFS A12379 or A12380, respectively) for 1 hour. Wells were washed by dilution in PBSTx, taking care to keep the cell-particle conjugates fully submerged in fluid throughout. For live imaging experiments, wells with beads were first mounted onto an inverted microscope stage and temperature-equilibrated for 15 to 30 min, after which 0.5 to  $1\times 10^5$  Lifeact-eGFP+ or Lamp1-eGFP+ CTLs were deposited into the wells and imaged.

Instant structured illumination microscopy (iSIM) was performed on an Olympus IX-73 microscope equipped with a VisiTech iSIM scan head (VisiTech International), an Optospin fast filter wheel (Cairn), a 60× 1.3-numerical aperture (NA) silicone oil objective (Olympus), and a Hamamatsu Flash 4.0 v2 camera. For livecell imaging, heating, humidity, and CO2 levels were maintained using a WSKM-F1 stage top incubator (Tokai Hit). Images were acquired using MetaMorph software (Molecular Devices). Conjugates were identified morphologically by cell polarization toward the bead and F-actin accumulation at the contact region. Image stacks were captured using 0.3-µm z-sectioning (80 to 120 slices per stack). In general, the 488-nm laserline (OBIS LX/LS, Coherent) was used to image phalloidin/Lifeact-eGFP/Lamp1-eGFP, and the 563-nm laserline (OBIS LX/LS, Coherent) was used to visualize the DAAM particle. For movie S3, images were acquired every  $\Delta t = 3$  min; for movie S2,  $\Delta t = 1$  min; for Movie S1,  $\Delta t = 15$  s; and for degranulation experiments (e.g., Fig. 2 and movie S4),  $\Delta t = 1$  min. For the experiments shown in Fig. 8 and fig. S13, fixed CTL-DAAM particle conjugates were imaged on a Leica Stellaris 8 laser scanning confocal microscope fitted with a white light laser, a 63× 1.4-NA objective lens, an Acousto-optical beam splitter, and HyD detector. Special care was taken to acquire images with a voxel size  $(109 \times 109 \times 300 \text{ nm}^3)$ matching the iSIM data. For all downstream image analysis, raw images were used as the input with no image deconvolution.

### Microparticle 3D shape reconstruction and contact area selection

3D particle reconstruction was conducted using a previously described custom MATLAB script (20). Briefly, individual microparticles were segmented by intensity thresholding on z-stacks, then particle edges were detected using the 3D Sobel operator and superlocalized by Gaussian fitting. This process yielded a set of i points p, representing the edge coordinates of the particle. Each p could be represented as Cartesian coordinates

$$p_i = [p_{i,x}, p_{i,y}, p_{i,z}]$$

or as spherical coordinates, with the origin set to the centroid of the particle:

$$p_i = [p_{i,\theta}, p_{i,\varphi}, p_{i,\rho}]$$

These point sets were triangulated using a convex hull approach to connect all edge coordinates without leaving gaps. At each node of the triangulated mesh, the first two principal curvatures ( $k_1$  and  $k_2$ ) were determined and then used to calculate mean curvature H.

$$H_i = \frac{k_1 + k_2}{2}$$

Contact areas were identified as regions of interest (ROIs) on the basis of the fluorescence intensity of phalloidin-stained F-actin in contact with the particle. The bounds of this ROI were defined by the  $\theta$  and  $\phi$  coordinates enclosing the F-actin–rich region. After cell-contact demarcation, all edge coordinates within the ROI were isolated to define the contact area of interest for downstream analysis.

#### **Zernike decomposition**

Zernike polynomials are orthogonal to each other over a unit circle. Thus, any function on a unit circle  $f(r, \theta)$  can be expressed as a sum of Zernike functions, in a manner similar to a 1D Fourier transform:

$$f(r,\theta) = \sum_{n=0}^{\infty} \sum_{m=-n}^{n} a_{n,m} Z_n^m(r,\theta)$$

where  $a_{n,m}$  is the modal coefficient associated with the Zernike polynomial of the nth degree and mth order,  $Z_n^m$ . Zernike polynomials comprise an infinite set of orthogonal functions, so to numerically calculate the modal coefficients, we truncated the set to a predefined N degrees:

$$f(r,\theta) \approx \sum_{n=0}^{N} \sum_{m=-n}^{n} a_{n,m} Z_n^m(r,\theta)$$

We used N=15 for most analyses because this generated a faithful reconstruction of topographies while avoiding overfitting (fig. S14). To numerically compute the modal coefficients for a 50 × 50 topography matrix M, we removed all data outside of the unit circle, linearized the remaining data into a discretized function vector  $F(r_i, \theta_i)$ , and then computed the Zernike polynomials up to N degrees on the gridded data point locations  $Z(r_i, \theta_i)$  via the MATLAB zernfun function (67). This yielded the following overdetermined system of linear equations,

$$F(r_i, \theta_i) = \sum_{n=0}^{N} \sum_{m=-n}^{n} a_{n,m} Z_n^m(r_i, \theta_i)$$

which we solved using the MATLAB left matrix division operator, producing Zernike modal coefficients  $a_{n,m}$ . Critically, although the degree n and absolute value of the order m define the shape and frequency of the Zernike polynomials, the sign of m determines their azimuthal rotation. Thus, the relative weighting of coefficients  $a_{n,m}$  and  $a_{n,-m}$  only provide rotational information. We assumed that force exertion patterns are rotationally degenerate, i.e., two patterns that are identical except for their azimuthal (en face) rotation are functionally identical. Thus, we reduced the modal coefficients a to an azimuthally degenerate set of a

$$C_{n,m} = \sqrt{a_{n,m}^2 + a_{n,-m}^2}$$

Rotational information is lost at this step, and thus the original pattern  $F(r_i, \theta_i)$  cannot be reconstructed from C. We used the azimuthally degenerate spectral coefficients C as feature vectors in PCA using the MATLAB pca function. Each  $50 \times 50$  gridded synapse  $M_i$  was transformed into coefficient vector  $C_i$ . The vectors were then concatenated into a matrix with each column corresponding

to one synapse and each row corresponding to the index of *C*. The output principal components scores, loadings, and explained variance were then truncated to the first two principal components and visualized as a scatter plot.

#### **Computation of spectral complexity**

Using modal Zernike coefficients  $a_{n,m}$ , we can approximately reconstruct the original data:

$$F_{\text{reconstructed}}(r_i, \theta_i) = \sum_{n=-1}^{N} \sum_{n=-1}^{n} a_{n,m} Z_n^m(r_i, \theta_i)$$

The correlation between the original data  $F(r_i, \theta_i)$  and the reconstructed estimate  $F_{\text{reconstructed}}(r_i, \theta_i)$  increases asymptotically with N (see fig. S7A):

$$\lim_{N \to \infty} F_{\text{reconstructed}}(r_i, \theta_i) - F(r_i, \theta_i) = 0$$

Although this necessarily holds true for all synapses, the exact shape of this curve can only be determined empirically and is dependent on the underlying complexity of the data. For example, very simple patterns with low-frequency undulations converge to near-perfect reconstruction relatively quickly using only a few Zernike polynomials, whereas complex, high frequency undulations require higher-order polynomials to achieve the same reconstruction accuracy (fig. S7B). We defined a spectral complexity parameter based on the Zernike transform as the area over the curve (AOC) in a reconstruction plot of Pearson's correlation coefficient (R) versus radial degree (N) for a given topography. To calculate spectral complexity, we first computed modal coefficients as described above iteratively, increasing from N = 1 to N = 40. At each iteration, the computed coefficients were multiplied by their respective Zernike functions to compute  $F_{\text{reconstructed}}(r_i, \theta_i)$ . Pearson's correlation between  $F_{\text{reconstructed}}(r_i, \theta_i)$  and the discretized topography matrix  $F(r_i, \theta_i)$  $\theta_i$ ) was calculated using the MATLAB corr2 function. The spectral complexity was calculated as the integrated sum of the R-N plot (calculated using the MATLAB trapz function), subtracted from  $N_{\text{max}} = 40$  (corresponding to the AOC).

For statistical analysis of spectral complexity values across samples, we used permutation testing to assess statistical significance, which obviated the need to assume a uniform distribution for the null hypothesis. Bootstrap resampling was used to generate  $10^5$  random permutations of the samples in each group. Then, the absolute difference in the means between permuted groups was computed as the test statistic to generate an empirical null distribution. The measured difference in means ( $|\Delta\mu_{actual}|$ ) between experimental groups was computed and a P value calculated as the proportion of the null distribution greater than  $|\Delta\mu_{actual}|$  (fig. S15). For experiments with multiple comparisons, false discovery rates (FDRs) were computed using the Benjamini-Hochberg method, and differences between experimental groups were deemed statistically significant for FDR < 0.05.

#### Statistical analysis

Figure panels show representative experiments, with the exception of Figs. 5, D, F, and G; 6, B, C, E, and F; and 8, C, F, and G; and figs. S8, A to D; S10, A to C and I S11, B to F and J; and S13, A and C, which show pooled data from all biological replicates. Analysis was performed using either representative experiments or pooled

data as indicated. *T* tests and permutation testing were performed in MATLAB. Error bars denote SD or SEM as noted in the figure captions.

#### **Supplementary Materials**

The PDF file includes:

Materials and Methods Figs. S1 to S15 Tables S1 and S2 References (68–81)

Other Supplementary Material for this manuscript includes the following:

Movies S1 to S4

Data file S1

MDAR Reproducibility Checklist

#### **REFERENCES AND NOTES**

- T. Iskratsch, H. Wolfenson, M. P. Sheetz, Appreciating force and shape-the rise of mechanotransduction in cell biology. Nat. Rev. Mol. Cell Biol. 15, 825–833 (2014).
- T. Mammoto, A. Mammoto, D. E. Ingber, Mechanobiology and developmental control. Annu. Rev. Cell Dev. Biol. 29, 27–61 (2013).
- M. Wall, D. Butler, A. El Haj, J. C. Bodle, E. G. Loboa, A. J. Banes, Key developments that impacted the field of mechanobiology and mechanotransduction. J. Orthop. Res. 36, 605–619 (2018).
- D.T. Butcher, T. Alliston, V. M. Weaver, A tense situation: Forcing tumour progression. Nat. Rev. Cancer 9, 108–122 (2009).
- 5. J. E. Moore Jr., C. D. Bertram, Lymphatic system flows. *Annu. Rev. Fluid Mech.* **50**, 459–482
- M. Huse, Mechanical forces in the immune system. Nat. Rev. Immunol. 17, 679–690 (2017).
- F. Y. McWhorter, C. T. Davis, W. F. Liu, Physical and mechanical regulation of macrophage phenotype and function. Cell. Mol. Life Sci. 72, 1303–1316 (2015).
- D. Blumenthal, V. Chandra, L. Avery, J. K. Burkhardt, Mouse T cell priming is enhanced by maturation-dependent stiffening of the dendritic cell cortex. eLife 9, e55995 (2020).
- D. Friedman, P. Simmonds, A. Hale, L. Bere, N. W. Hodson, M. R. H. White, D. M. Davis, Natural killer cell immune synapse formation and cytotoxicity are controlled by tension of the target interface. *J. Cell Sci.* 134, jcs258570 (2021).
- E. Judokusumo, E. Tabdanov, S. Kumari, M. L. Dustin, L. C. Kam, Mechanosensing in T lymphocyte activation. *Biophys. J.* 102, L5–L7 (2012).
- Z. Wan, S. Zhang, Y. Fan, K. Liu, F. Du, A. M. Davey, H. Zhang, W. Han, C. Xiong, W. Liu, B cell activation is regulated by the stiffness properties of the substrate presenting the antigens. *J. Immunol.* 190, 4661–4675 (2013).
- A. G. Solis, P. Bielecki, H. R. Steach, L. Sharma, C. C. D. Harman, S. Yun, M. R. de Zoete, J. N. Warnock, S. D. F. To, A. G. York, M. Mack, M. A. Schwartz, C. S. Dela Cruz, N. W. Palm, R. Jackson, R. A. Flavell, Author correction: Mechanosensation of cyclical force by PIEZO1 is essential for innate immunity. *Nature* 573, 69–74 (2019).
- K. P. Meng, F. S. Majedi, T. J. Thauland, M. J. Butte, Mechanosensing through YAP controls T cell activation and metabolism. J. Exp. Med. 217, e20200053 (2020).
- M. Saitakis, S. Dogniaux, C. Goudot, N. Bufi, S. Asnacios, M. Maurin, C. Randriamampita, A. Asnacios, C. Hivroz, Different TCR-induced T lymphocyte responses are potentiated by stiffness with variable sensitivity. *eLife* 6, e23190 (2017).
- H. D. Moreau, C. Blanch-Mercader, R. Attia, M. Maurin, Z. Alraies, D. Sanseau, O. Malbec, M. G. Delgado, P. Bousso, J. F. Joanny, R. Voituriez, M. Piel, A. M. Lennon-Dumenil, Macropinocytosis overcomes directional bias in dendritic cells due to hydraulic resistance and facilitates space exploration. *Dev. Cell* 49, 171–188.e5 (2019).
- J. Renkawitz, A. Kopf, J. Stopp, I. de Vries, M. K. Driscoll, J. Merrin, R. Hauschild, E. S. Welf, G. Danuser, R. Fiolka, M. Sixt, Nuclear positioning facilitates amoeboid migration along the path of least resistance. *Nature* 568, 546–550 (2019).
- A. Reversat, F. Gaertner, J. Merrin, J. Stopp, S. Tasciyan, J. Aguilera, I. de Vries, R. Hauschild, M. Hons, M. Piel, A. Callan-Jones, R. Voituriez, M. Sixt, Cellular locomotion using environmental topography. *Nature* 582, 582–585 (2020).
- V. Jaumouille, A. X. Cartagena-Rivera, C. M. Waterman, Coupling of β2 integrins to actin by a mechanosensitive molecular clutch drives complement receptor-mediated phagocytosis. Nat. Cell Biol. 21, 1357–1369 (2019).
- D. Vorselen, R. A. Kamber, R. L. D. Labitigan, A. P. van Loon, E. Peterman, M. K. Delgado, S. Lin, J. P. Rasmussen, M. C. Bassik, J. A. Theriot, Cell surface receptors TREM2, CD14 and integrin α<sub>M</sub>β<sub>2</sub> drive sinking engulfment in phosphatidylserine-mediated phagocytosis. bioRxiv [Preprint] (2022); https://doi.org/10.1101/2022.07.30.502145.
- D. Vorselen, Y. Wang, M. M. de Jesus, P. K. Shah, M. J. Footer, M. Huse, W. Cai, J. A. Theriot, Microparticle traction force microscopy reveals subcellular force exertion patterns in immune cell-target interactions. *Nat. Commun.* 11, 20 (2020).

### SCIENCE IMMUNOLOGY | RESEARCH ARTICLE

- L. J. Dooling, J. C. Andrechak, B. H. Hayes, S. Kadu, W. Zhang, R. Pan, M. Vashisth, J. Irianto, C. M. Alvey, L. Ma, D. E. Discher, Cooperative phagocytosis of solid tumours by macrophages triggers durable anti-tumour responses. *Nat. Biomed. Eng.* 7, 1081–1096 (2023).
- D. Vorselen, S. R. Barger, Y. Wang, W. Cai, J. A. Theriot, N. C. Gauthier, M. Krendel, Phagocytic 'teeth' and myosin-II 'jaw' power target constriction during phagocytosis. *eLife* 10, e68627 (2021).
- E. Natkanski, W. Y. Lee, B. Mistry, A. Casal, J. E. Molloy, P. Tolar, B cells use mechanical energy to discriminate antigen affinities. *Science* 340, 1587–1590 (2013).
- K. M. Spillane, P. Tolar, Mechanisms of B cell antigen extraction revealed by DNA-based molecular sensors. *Biophys. J.* 110, 511a–512a (2016).
- A. Kumari, J. Pineau, P. J. Saez, M. Maurin, D. Lankar, M. San Roman, K. Hennig,
   V. F. Boura, R. Voituriez, M. C. I. Karlsson, M. Balland, A. M. L. Dumenil, P. Pierobon,
   Actomyosin-driven force patterning controls endocytosis at the immune synapse. *Nature* 10, 2870 (2019)
- R. Basu, B. M. Whitlock, J. Husson, A. Le Floc'h, W. Jin, A. Oyler-Yaniv, F. Dotiwala, G. Giannone, C. Hivroz, N. Biais, J. Lieberman, L. C. Kam, M. Huse, Cytotoxic T cells use mechanical force to potentiate target cell killing. Cell 165, 100–110 (2016).
- I. Voskoboinik, J. C. Whisstock, J. A. Trapani, Perforin and granzymes: Function, dysfunction and human pathology. Nat. Rev. Immunol. 15, 388–400 (2015).
- X. Liu, J. Lieberman, Knocking 'em dead: Pore-forming proteins in immune defense. Annu. Rev. Immunol. 38, 455–485 (2020).
- M. S. Wang, Y. Hu, E. E. Sanchez, X. Xie, N. H. Roy, M. de Jesus, B. Y. Winer, E. A. Zale, W. Jin, C. Sachar, J. H. Lee, Y. Hong, M. Kim, L. C. Kam, K. Salaita, M. Huse, Mechanically active integrins target lytic secretion at the immune synapse to facilitate cellular cytotoxicity. *Nat. Commun.* 13, 3222 (2022).
- F. Tamzalit, M. S. Wang, W. Jin, M. Tello-Lafoz, V. Boyko, J. M. Heddleston, C. T. Black, L. C. Kam, M. Huse, Interfacial actin protrusions mechanically enhance killing by cytotoxic T cells. Sci. Immunol. 4, eaav5445 (2019).
- A. G. York, P. Chandris, D. D. Nogare, J. Head, P. Wawrzusin, R. S. Fischer, A. Chitnis, H. Shroff, Instant super-resolution imaging in live cells and embryos via analog image processing. *Nat. Methods* 10, 1122–1126 (2013).
- E. E. Sanchez, M. Tello-Lafoz, A. J. Guo, M. de Jesus, Y. A. Elbanna, B. Y. Winer, S. Budhu, E. Chan, E. Rosiek, T. Kondo, J. DuSold, N. Taylor, G. Altan-Bonnet, M. F. Olson, M. Huse, Apoptotic contraction drives target cell release by cytotoxic T cells. *Nat. Immunol.* 24, 1434–1442 (2023)
- G. D. Rak, E. M. Mace, P. P. Banerjee, T. Svitkina, J. S. Orange, Natural killer cell lytic granule secretion occurs through a pervasive actin network at the immune synapse. *PLoS Biol.* 9, e1001151 (2011).
- A. C. Brown, S. Oddos, I. M. Dobbie, J. M. Alakoskela, R. M. Parton, P. Eissmann, M. A. Neil, C. Dunsby, P. M. French, I. Davis, D. M. Davis, Remodelling of cortical actin where lytic granules dock at natural killer cell immune synapses revealed by super-resolution microscopy. *PLoS Biol.* 9, e1001152 (2011).
- A.T. Ritter, Y. Asano, J. C. Stinchcombe, N. M. Dieckmann, B. C. Chen, C. Gawden-Bone,
   S. van Engelenburg, W. Legant, L. Gao, M. W. Davidson, E. Betzig, J. Lippincott-Schwartz,
   G. M. Griffiths, Actin depletion initiates events leading to granule secretion at the immunological synapse. *Immunity* 42, 864–876 (2015).
- J. C. Stinchcombe, G. M. Griffiths, Secretory mechanisms in cell-mediated cytotoxicity. *Annu. Rev. Cell Dev. Biol.* 23, 495–517 (2007).
- M. A. Govendir, D. Kempe, S. Sianti, J. Cremasco, J. K. Mazalo, F. Colakoglu, M. Golo, K. Poole, M. Biro, T cell cytoskeletal forces shape synapse topography for targeted lysis via membrane curvature bias of perforin. *Dev. Cell* 57, 2237–2247.e8 (2022).
- A. V. Lotov, K. Miettinen, "Visualizing the Pareto frontier" in Multiobjective Optimization: Lecture Notes in Computer Science, J. Branke, K. Deb, K. Miettinen, R. Slowinski, Eds. (Springer, Berlin, 2008), pp. 213–243.
- K. I. Jankowska, E. K. Williamson, N. H. Roy, D. Blumenthal, V. Chandra, T. Baumgart,
  J. K. Burkhardt, Integrins modulate T cell receptor signaling by constraining actin flow at
  the immunological synapse. Front. Immunol. 9, 25 (2018).
- C. Kim, F. Ye, M. H. Ginsberg, Regulation of integrin activation. Annu. Rev. Cell Dev. Biol. 27, 321–345 (2011).
- F. Zernike, Beugungstheorie des schneidenver-fahrens und seiner verbesserten form, der phasenkontrastmethode. Phys. Ther. 1, 689–704 (1934).
- 42. V. Capalbo, M. De Petris, F. De Luca, W. Cui, G. Yepes, A. Knebe, E. Rasia, Clusters morphology by Zernike polynomials. *Nuovo Cimento C.* **44**, 1–4 (2021).
- N. Vladimirov, X. Tao, "Adaptive optics" in *Imaging Modalities for Biological and Preclinical Research: Part 1: Ex Vivo Biological Imaging*, A. Walter, J. G. Mannheim, C. J. Caruana, Eds. (IOP Publishing, United Kingdom, 2021), pp. 1.2.e-1 to 1.2.e-11.
- A. Le Floc'h, Y. Tanaka, N. S. Bantilan, G. Voisinne, G. Altan-Bonnet, Y. Fukui, M. Huse, Annular PIP3 accumulation controls actin architecture and modulates cytotoxicity at the immunological synapse. *J. Exp. Med.* 210, 2721–2737 (2013).
- T. S. Gourley, E. J. Wherry, D. Masopust, R. Ahmed, Generation and maintenance of immunological memory. Semin. Immunol. 16, 323–333 (2004).

- M. Philip, A. Schietinger, Heterogeneity and fate choice: T cell exhaustion in cancer and chronic infections. *Curr. Opin. Immunol.* 58, 98–103 (2019).
- E. J. Wherry, M. Kurachi, Molecular and cellular insights into T cell exhaustion. Nat. Rev. Immunol. 15, 486–499 (2015).
- 48. D. Zehn, E. J. Wherry, Immune memory and exhaustion: Clinically relevant lessons from the LCMV model. *Adv. Exp. Med. Biol.* **850**, 137–152 (2015).
- S. M. Kaech, S. Hemby, E. Kersh, R. Ahmed, Molecular and functional profiling of memory CD8 T cell differentiation. Cell 111, 837–851 (2002).
- E. J. Wherry, J. N. Blattman, K. Murali-Krishna, R. van der Most, R. Ahmed, Viral persistence alters CD8 T-cell immunodominance and tissue distribution and results in distinct stages of functional impairment. J. Virol. 77, 4911–4927 (2003).
- A. J. Zajac, J. N. Blattman, K. Murali-Krishna, D. J. Sourdive, M. Suresh, J. D. Altman, R. Ahmed, Viral immune evasion due to persistence of activated T cells without effector function. J. Exp. Med. 188, 2205–2213 (1998).
- M. F. Bachmann, M. Barner, A. Viola, M. Kopf, Distinct kinetics of cytokine production and cytolysis in effector and memory T cells after viral infection. *Eur. J. Immunol.* 29, 291–299 (1999).
- N. D. Barth, J. A. Marwick, M. Vendrell, A. G. Rossi, I. Dransfield, The "phagocytic synapse" and clearance of apoptotic cells. Front. Immunol. 8, 1708 (2017).
- F. Niedergang, V. Di Bartolo, A. Alcover, Comparative anatomy of phagocytic and immunological synapses. Front. Immunol. 7, 18 (2016).
- S. R. Barger, D. Vorselen, N. C. Gauthier, J. A. Theriot, M. Krendel, F-actin organization and target constriction during primary macrophage phagocytosis is balanced by competing activity of myosin-I and myosin-II. *Mol. Biol. Cell* 33, br24 (2022).
- A. M. Beal, N. Anikeeva, R. Varma, T. O. Cameron, G. Vasiliver-Shamis, P. J. Norris,
   M. L. Dustin, Y. Sykulev, Kinetics of early T cell receptor signaling regulate the pathway of lytic granule delivery to the secretory domain. *Immunity* 31, 632–642 (2009).
- S. Vanni, H. Hirose, H. Barelli, B. Antonny, R. Gautier, A sub-nanometre view of how membrane curvature and composition modulate lipid packing and protein recruitment. *Nat. Commun.* 5, 4916 (2014).
- E. J. Wherry, S. J. Ha, S. M. Kaech, W. N. Haining, S. Sarkar, V. Kalia, S. Subramaniam, J. N. Blattman, D. L. Barber, R. Ahmed, Molecular signature of CD8<sup>+</sup>T cell exhaustion during chronic viral infection. *Immunity* 27, 670–684 (2007).
- I. Prager, C. Liesche, H. van Ooijen, D. Urlaub, Q. Verron, N. Sandstrom, F. Fasbender, M. Claus, R. Eils, J. Beaudouin, B. Onfelt, C. Watzl, NK cells switch from granzyme B to death receptor-mediated cytotoxicity during serial killing. *J. Exp. Med.* 216, 2113–2127 (2019).
- A. Crawford, J. M. Angelosanto, C. Kao, T. A. Doering, P. M. Odorizzi, B. E. Barnett, E. J. Wherry, Molecular and transcriptional basis of CD4<sup>+</sup>T cell dysfunction during chronic infection. *Immunity* 40, 289–302 (2014).
- J. L. Daniel, I. R. Molish, L. Robkin, H. Holmsen, Nucleotide exchange between cytosolic ATP and F-actin-bound ADP may be a major energy-utilizing process in unstimulated platelets. Eur. J. Biochem. 156, 677–683 (1986).
- B. W. Bernstein, J. R. Bamburg, Actin-ATP hydrolysis is a major energy drain for neurons. J. Neurosci. 23, 1–6 (2003).
- J. A. Champion, S. Mitragotri, Role of target geometry in phagocytosis. Proc. Natl. Acad. Sci. U.S.A. 103, 4930–4934 (2006).
- A. H. Settle, B. Y. Winer, M. M. de Jesus, L. Seeman, Z. Wang, E. Chan, Y. Romin, Z. Li, M. M. Miele, R. C. Hendrickson, D. Vorselen, J. S. A. Perry, M. Huse, β2 integrins impose a mechanical checkpoint on macrophage phagocytosis. bioRxiv [Preprint] (2024); https://doi.org/10.1101/2024.02.20.580845.
- C. McQuin, A. Goodman, V. Chernyshev, L. Kamentsky, B. A. Cimini, K. W. Karhohs, M. Doan, L. Y. Ding, S. M. Rafelski, D. Thirstrup, W. Wiegraebe, S. Singh, T. Becker, J. C. Caicedo, A. E. Carpenter, CellProfiler 3.0: Next-generation image processing for biology. *PLoS Biol.* 16, e2005970 (2018).
- S. B. Kotsiantis, Supervised machine learning: A review of classification techniques. Informatica 31, 249–268 (2007).
- 67. P. Fricker, Zernike polynomials. MATLAB Central File Exchange (2024); https://www.mathworks.com/matlabcentral/fileexchange/7687-zernike-polynomials.
- J. Riedl, A. H. Crevenna, K. Kessenbrock, J. H. Yu, D. Neukirchen, M. Bista, F. Bradke,
   D. Jenne, T. A. Holak, Z. Werb, M. Sixt, R. Wedlich-Soldner, Lifeact: A versatile marker to visualize F-actin. *Nat. Methods* 5, 605–607 (2008).
- R. J. Platt, S. Chen, Y. Zhou, M. J. Yim, L. Swiech, H. R. Kempton, J. E. Dahlman, O. Parnas, T. M. Eisenhaure, M. Jovanovic, D. B. Graham, S. Jhunjhunwala, M. Heidenreich, R. J. Xavier, R. Langer, D. G. Anderson, N. Hacohen, A. Regev, G. Feng, P. A. Sharp, F. Zhang, CRISPR-Cas9 knockin mice for genome editing and cancer modeling. *Cell* 159, 440–455 (2014).
- N. E. Sanjana, O. Shalem, F. Zhang, Improved vectors and genome-wide libraries for CRISPR screening. Nat. Methods 11, 783–784 (2014).
- C. Fellmann, T. Hoffmann, V. Sridhar, B. Hopfgartner, M. Muhar, M. Roth, D. Y. Lai,
   I. A. Barbosa, J. S. Kwon, Y. Guan, N. Sinha, J. Zuber, An optimized microRNA backbone for effective single-copy RNAi. *Cell Rep.* 5, 1704–1713 (2013).

### SCIENCE IMMUNOLOGY | RESEARCH ARTICLE

- J. Weischenfeldt, B. Porse, Bone marrow-derived macrophages (BMM): Isolation and applications. CSH Protoc. 2008, pdb.prot5080 (2008).
- R. H. Pullen III, S. M. Abel, Catch bonds at T cell interfaces: Impact of surface reorganization and membrane fluctuations. *Biophys. J.* 113, 120–131 (2017).
- S. Y. Qi, J. T. Groves, A. K. Chakraborty, Synaptic pattern formation during cellular recognition. Proc. Natl. Acad. Sci. U.S.A. 98, 6548–6553 (2001).
- Z. Zhang, T. K. Gaetjens, J. Ou, Q. Zhou, Y. Yu, D. P. Mallory, S. M. Abel, Y. Yu, Propulsive cell entry diverts pathogens from immune degradation by remodeling the phagocytic synapse. Proc. Natl. Acad. Sci. U.S.A. 120, e2306788120 (2023).
- R. K. Sadhu, C. Hernandez-Padilla, Y. E. Eisenbach, S. Penic, L. Zhang, H. D. Vishwasrao, B. Behkam, K. Konstantopoulos, H. Shroff, A. Iglic, E. Peles, A. S. Nain, N. S. Gov, Experimental and theoretical model for the origin of coiling of cellular protrusions around fibers. *Nat. Commun.* 14, 5612 (2023).
- J. E. Hassinger, G. Oster, D. G. Drubin, P. Rangamani, Design principles for robust vesiculation in clathrin-mediated endocytosis. *Proc. Natl. Acad. Sci. U.S.A.* 114, E1118–E1127 (2017).
- A. E. Carlsson, Membrane bending by actin polymerization. Curr. Opin. Cell Biol. 50, 1–7 (2018).
- H. J. Lee, E. L. Peterson, R. Phillips, W. S. Klug, P. A. Wiggins, Membrane shape as a reporter for applied forces. Proc. Natl. Acad. Sci. U.S.A. 105, 19253–19257 (2008).
- M. Deserno, Fluid lipid membranes: From differential geometry to curvature stresses. Chem. Phys. Lipids 185, 11–45 (2015).
- J. El-Beyrouthy, M. M. Makhoul-Mansour, G. Taylor, S. A. Sarles, E. C. Freeman, A new approach for investigating the response of lipid membranes to electrocompression by coupling droplet mechanics and membrane biophysics. J. R. Soc. Interface 16, 20190652 (2019).

Acknowledgments: We thank C. Firl, L. Stafford, C. Jeronimo, N. Lovinger, and A. Yakimov for technical support; the Flow Cytometry Core Facility for assistance with FACS; A. Schietinger for the LCMV; and P. Niethammer, S. Rudensky, W. Tansey, and members of the M.H., Z.B., J.C.S., and J.A.T. labs for advice. Funding: This work was supported in part by the NIH (R01-Al087644 to M.H., R01-Al100874 to J.C.S., and P30-CA008748 to MSKCC), the Ludwig Foundation for Cancer Immunotherapy (M.d.J.), the National Science Foundation (PHY-1753017 to S.M.A. and a Graduate Research Fellowship to A.H.S.), the Howard Hughes Medical Institute (to J.A.T.), the Schmidt Science Fellows Program (B.Y.W.), and the Cancer Research Institute (B.Y.W.). Author contributions: M.d.J., A.H.S., T.K.G., E.S., B.Y.W., J.C.S., S.M.A., and M.H. designed the experiments. M.d.J., A.H.S., T.K.G., E.S., E.L., M.G., Y.Y.W., and M.H. collected the data. M.d.J., A.H.S., T.K.G., E.S., E.L., S.M.A., and M.H. analyzed the data. D.V., F.T., and M.S.W. generated key reagents, M.G., Y.R., T.-M.F., A.S., P.S., D.V., and J.A.T. provided critical input with imaging experiments and image analysis. Z.B., J.C.S., J.A.T., S.M.A., and M.H. provided research support. M.d.J., A.H.S., and M.H. wrote the paper. **Competing interests:** The authors declare that they have no competing interests. Data and materials availability: Tabulated data underlying the figures are provided in data file S1. The custom MATLAB code used for analysis can be found at https://zenodo.org/records/11123095. All other data needed to support the conclusions of the paper are present in the paper or the Supplementary Materials. All reagents used in this study are available via a materials transfer agreement, and requests for reagents should be addressed to M.H. (husem@mskcc.org).

Submitted 17 June 2023 Resubmitted 22 March 2024 Accepted 5 June 2024 Published 28 June 2024 10.1126/sciimmunol.adj2898